Setting up an *In Vitro* Reconstitution System to Study Actomyosin-Driven Membrane Organisation

Master's Thesis submitted to the Indian Institute of Science Education and Research Pune in partial fulfilment of the requirements for the BS-MS Dual Degree Programme

By

Likhith Chandragiri
(Reg. No. 20191173)

Indian Institute of Science Education and Research Pune
Dr. Homi Bhabha Road, Pashan, Pune 411008, INDIA.

April 2024

Under the supervision of **Prof. Satyajit Mayor**
at the **National Centre for Biological Sciences (NCBS)**

From May 2023 to March 2024

Certificate

This is to certify that this dissertation entitled "**Setting up an *In Vitro* Reconstitution System to Study Actomyosin-Driven Membrane Organisation**", submitted towards the partial fulfilment of the BS-MS dual degree programme at the Indian Institute of Science Education and Research, Pune represents study/work carried out by Likhith Chandragiri at the National Centre for Biological Sciences under the supervision of Prof. Satyajit Mayor, during the academic year 2023-24.

Prof. Satyajit Mayor

Committee:

Supervisor: Prof. Satyajit Mayor
Expert: Prof. Thomas Pucadyil

This thesis is dedicated to my family
for their patience, love and support

Declaration

I hereby declare that the matter embodied in the report entitled "**Setting up an *In Vitro* Reconstitution System to Study Actomyosin-Driven Membrane Organisation**" are the results of the work carried out by me at the National Centre for Biological Sciences under the supervision of Prof. Satyajit Mayor and the same has not been submitted elsewhere for any other degree. Wherever others contribute, every effort is made to indicate this clearly, with due reference to the literature and acknowledgement of collaborative research and discussions.

Likhith Chandragiri
Reg. no. 20191173

Table of Contents

List of Figures

List of Tables

Symbols and Notations

ADU: Analog to Digital Unit

ATP: Adenosine Triphosphate

BME: Beta-mercaptoethanol

CapZ: Capping Protein

DGS-NTA(Ni): 1,2-Dioleoyl-sn-glycero-3-[(N-(5-amino-1-carboxypentyl)iminodiacetic acid)succinyl] (nickel salt)

DOPC: 1,2-Dioleoyl-sn-glycero-3-phosphocholine

DTT: Dithiothreitol

EGFP: Enhanced Green Fluorescent Protein

EGTA: Ethylene Glycol Tetraacetic Acid

ELC: Non-Muscle Myosin II Essential Light Chain

EzrinABD: Ezrin Actin-Binding Domain

FRAP: Fluorescence Recovery After Photobleaching

GPI: Glycosylphosphatidylinositol

GPMV: Giant Plasma Membrane Vesicle

GUV: Giant Unilamellar Vesicle

IPTG: Isopropyl ß-D-1-thiogalactopyranoside

LB: Luria-Bertani Broth

MLCK: Myosin Light Chain Kinase

MLV: Multilamellar Vesicle

MOPS: 3-(N-morpholino) Propanesulfonic Acid

NA: Numerical Aperture

NMII: Non-Muscle Myosin II

NMIIA-HC: Non-Muscle Myosin IIA Heavy Chain

NMIIA: Non-Muscle Myosin IIA

NMIIB-HC: Non-Muscle Myosin IIB Heavy Chain

NMIIB: Non-Muscle Myosin IIB

PBS: Phosphate-Buffered Saline

P_H: Polyhedrin Promoter

PMSF: Phenylmethylsulfonyl Fluoride

RLC: Non-Muscle Myosin II Regulatory Light Chain

ROI: Region of Interest

sCMOS: Scientific Complementary Metal–Oxide–Semiconductor Camera

SD: Standard Deviation

SDS: Sodium Dodecyl Sulfate

SOC: Super Optimal Broth with Catabolite Repression

STED: Stimulated Emission Depletion Microscopy

SUV: Small Unilamellar Vesicle

SV40 polyA: Simian Virus 40 Polyadenylation Sequence

TBST: Tris-buffered Saline with 0.1% Tween-20

TIRF: Total Internal Reflection Fluorescence Microscopy

UtrophinABD: Utrophin Actin-Binding Domain

ε: Molar Extinction Coefficient

λ: Wavelength

Abstract

The plasma membrane is the site of numerous crucial processes like signal transduction, cell adhesion and vesicular transport. These processes require the plasma membrane to be organised into distinct meso and nanoscale domains. Prevailing models of membrane organisation have neglected the role of the membrane-associated actin cortex in generating such domains through active, non-equilibrium processes. These models instead focus on passive, equilibrium processes emerging from protein-protein, lipid-protein and lipid-lipid interactions.

The Active Composite model emerged as an explanation for the non-equilibrium properties shown by certain membrane components like GPI-anchored proteins, which are largely inconsistent with the current paradigm of membrane organisation. The model predicts that actin-bound membrane components can undergo transient, active clustering as a consequence of ATP-driven actomyosin contractility. Previous work has shown that such clustering can occur *in vitro* due to the activity of skeletal muscle myosin II on pre-polymerised actin filaments. However, some caveats exist with this work. Actin filaments in cells are dynamic and undergo continuous treadmilling rather than being of fixed length. Moreover, skeletal muscle myosin II is a specialised motor that operates primarily in muscle cells. Non-muscle myosin II, on the other hand, is responsible for cytoplasmic actin contractility across eukaryotic cell types. The two myosins also differ in their length scales and motor activity kinetics.

Broadly, the aim of this thesis is to build an *in vitro* reconstitution system that better captures the dynamic nature of the membrane-associated actomyosin cortex by incorporating spontaneously polymerising dynamic actin filaments along with non-muscle myosin II motors. Such a system would be more suited to test the predictions of the Active Composite model. In this direction, I attempted to recombinantly express non-muscle myosin II as well as reconstitute spontaneously polymerising actin filaments on a supported lipid bilayer.

Acknowledgements

I express my sincere gratitude to Prof. Satyajit Mayor for giving me an opportunity to work on this exciting area of research. I am grateful for his valuable guidance, feedback and keen insight over the course of this project.

I also thank Bhagyashri Mahajan and Sankarshan Talluri for teaching me a variety of laboratory techniques, including recombinant protein expression in Sf9 cells and reconstitution of actin filaments over supported lipid bilayers. They provided me with necessary reagents, helped me conceptualise and troubleshoot experiments, and assisted me with microscopy. Next, I would like to thank Greeshma Pradeep for teaching me how to operate the TIRF microscope and helping me with characterising its properties, Pooja Krishna for helping out with western blots, and Shubhangi Sharma for helping with primer design. Further, I am grateful to Sarayu Beri, Chandrima Patra, and Dr. Sowmya Jahnavi for their invaluable support, advice and suggestions. I also thank Prof. James Sellers, Prof. Saravanan Palani and Jayanti Kumar for sharing essential resources without which this project would not have been possible.

I must also thank Prof. Thomas Pucadyil for being my internal expert, guiding me through numerous past projects, and introducing me to areas of membrane and cell biology. He has been a major source of guidance throughout my journey at IISER Pune. I also thank Prof. Girish Ratnaparkhi for his support, as well as Rakesh Mishra for his patience and counsel.

Lastly, I express my heartfelt gratitude to my family and friends for their love and support throughout this thesis and my journey at IISER Pune. I thank Shaswat Nair for being an absolutely integral part of my journey at IISER Pune and Yogen Borkar for his encouragement throughout this thesis. I am especially indebted to Ashli Jain for her kindness, friendship, and wisdom. This thesis would not have been possible without her unwavering support through trying times.

Contributions

Contributor name	Contributor role
LC, BM, SM, ST	Conceptualisation of Ideas
LC, BM, ST, GPS	Methodology
TVZ, GPS	Software
LC	Validation
LC	Formal analysis
LC	Investigation
LC, JK, SP, JS, BM, ST	Resources
LC	Data Curation
LC	Writing - original draft preparation
LC, SM	Writing - review and editing
LC	Visualisation
SM, BM, ST	Supervision
SM	Project administration
SM	Funding acquisition

LC: Likhith Chandragiri
BM: Bhagyashri Mahajan
ST: Sankarshan Talluri
SM: Satyajit Mayor
GPS: Greeshma Pradeep S
TVZ: Thomas van Zanten
JK: Jayanti Kumar
SP: Saravanan Palani
JS: James Sellers

This contributor syntax is based on the Journal of Cell Science CRediT Taxonomy[1].

[1] https://journals.biologists.com/jcs/pages/author-contributions

Chapter I: Introduction

The plasma membrane (PM) is a fluid mixture of lipids and proteins that defines the boundary of a cell, separating its contents from the surroundings and maintaining essential differences between the cytosol and extracellular milieu. The plasma membrane is the site of numerous crucial processes like cell adhesion, signal transduction and the uptake and release of cargo, allowing for the exchange of information and material between the cell and its surroundings. These processes require plasma membrane components to be organised into distinct nano-scale and meso-scale functional assemblies (Kusumi et al., 2012). However, we still do not have a complete understanding of the mechanisms by which this is reproducibly achieved (Rao and Mayor, 2014). Prevailing models of plasma membrane organisation assume that membrane components are maintained at thermodynamic equilibrium, organised by passive lipid-lipid, protein-lipid and protein-protein interactions (Rao and Mayor, 2014; Kalapurakkal et al., 2020). However, a growing number of observations of out-of-equilibrium properties of certain membrane components compels us to consider the role of active, non-equilibrium processes in organising the plasma membrane (Sharma *et al.,* 2004; Plowman et al*.,* 2005; Goswami et al*.,* 2008; Saha et al., 2015).

Fluid-Mosaic Model

The Fluid-Mosaic Model proposed by Singer and Nicholson in the 1970s was a significant attempt at synthesising experimental observations of the time into a visual representation of biological membranes (Edidin 2003a). Biological membranes were viewed as a well-mixed, equilibrated, fluid sea of lipids arranged in a bilayer with globular proteins randomly embedded in it (Singer and Nicholson, 1972) (Fig. 1A). However, we know today that the plasma membrane consists of non-random lateral heterogeneities that form specialised domains and structures. These structures exist across multiple scales, including signalling complexes, focal adhesions, lamellipodia, microvilli, polarised epithelia, etc. (Rao and Mayor, 2014). Moreover, we know today that lipids are asymmetrically arranged between the two leaflets of the membrane bilayer (Bretscher, 1972) and that membrane components can experience restrictions on their free diffusion (Kusumi et al*.,* 2012).

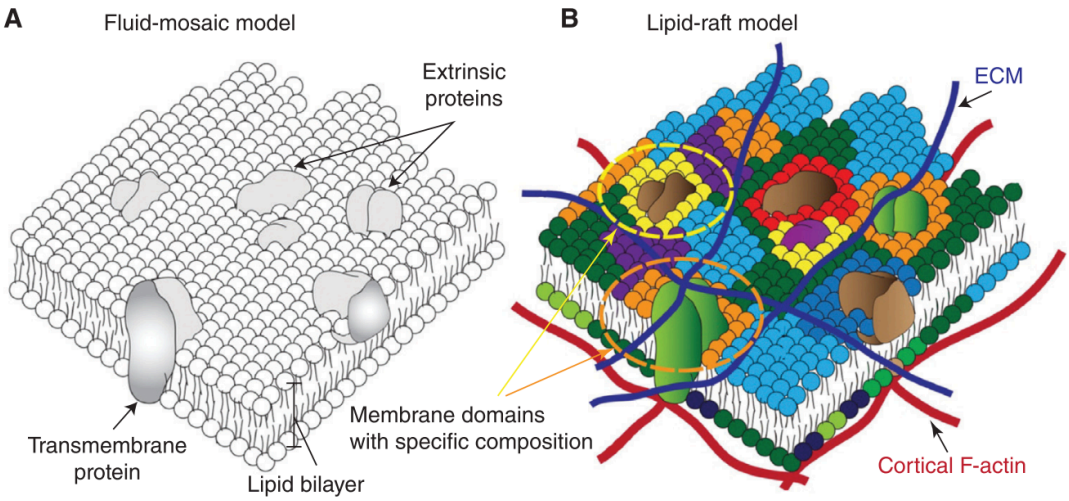

Fig. 1: Illustrations of (A) the Fluid Mosaic model depicting proteins embedded in a 'sea of lipids' and (B) the Lipid Raft model depicting heterogeneous membrane domains having specific lipid and protein compositions emerging from thermodynamic interactions (adapted from Mayor et al., 2023)

Lipid Raft Hypothesis

The lipid raft hypothesis emerged as an explanation for the requirement of laterally heterogeneous functional domains on the plasma membrane (Simons and Ikonen, 1997). The hypothesis originated from experiments on artificial membranes (GUVs) and plasma membrane-derived cell-free membranes (GPMVs) that were observed to undergo spontaneous micron-scale phase segregation into liquid-ordered (Lo) and liquid-disordered (Ld) domains due to passive lipid-lipid interactions (Edidin, 2003b). These domains are specifically enriched in certain kinds of lipids and exclude others, allowing for the preferential partitioning of proteins based on thermodynamic interactions (Fig. 1B). For example, Lo domains are enriched in cholesterol and sphingolipids, while Ld domains are cholesterol-poor (Edidin 2003b; Lingwood and Simons, 2010).

Cell membranes were thought to be similarly segregated to spontaneously form Lo-like platforms or 'rafts' into which proteins like GPI-anchored proteins could partition (Edidin,

2003b; Sezgin et al., 2017). The formation of these rafts was proposed as a general mechanism by which signalling, sorting and trafficking occur at the plasma membrane (Edidin, 2003b; Lingwood and Simons, 2010). However, evidence of such micron-scale assembly of Lo rafts has not been observed in living cells (Munro, 2003; Sezgin et al., 2017). Further, the micron-scale phase segregation into Lo and Ld domains occurs in GPMVs only when they are cooled to below physiological temperatures (Baumgart et al., 2007; Kaiser et al., 2009).

Importantly, classical lipid raft components like GPI-anchored proteins exist in nanoclusters in cells rather than larger assembles as predicted by the initial model (Varma and Mayor, 1998; Sharma et al., 2004). High-resolution measurements of these proteins and other canonical raft components in cells suggest that Lo-like structures on the plasma membrane are likely to be transient nanoscale assemblies (<20 nm), which are assembled to form larger structures (Lingwood and Simons, 2010; Mayor et al., 2023). However, the dynamics of GPI-anchored protein clusters on the plasma membrane are dependent on energy-consuming actomyosin dynamics (Gowrishankar et al., 2012), pointing towards active, non-equilibrium drivers of lateral heterogeneity in the membrane.

Anchored-Picket Fence Model

The Anchored-Picket Fence Model posits that the cortical actin cytoskeleton can impose restrictions on the free diffusion of plasma membrane components (Kusumi et al., 2012). Proteins and lipids in the membrane exhibit rapid diffusion in their immediate vicinity of a few nanometres but experience constrained diffusion at longer distances (Kusumi et al., 1993; Fujiwara et al., 2002). This is a consequence of the corralling of the membrane into mesoscale domains (40-300 nm), fenced by actin filaments and picketed by actin-binding transmembrane proteins (Fig. 2).

Actin filaments constrain the diffusion of transmembrane and inner leaflet proteins between domains, while picket proteins restrict the diffusion of lipids and outer leaflet proteins. The model suggests that these components can sometimes ‘hop’ between domains when there is a local separation or dispersal of actin filaments from the membrane, which manifests as a 20 times slower diffusion rate across length scales larger than 10 nm (Kusumi et al., 2012).

Within a corralled domain, this model allows for proteins to assemble into sub-mesoscale structures through protein-protein interactions or partition into phase-segregated rafts due to protein-lipid interactions (Kusumi et al., 2012). Importantly, this model constrains the size of rafts and provides a possibility by which oligomerisation of membrane components is promoted due to their compartmentalisation and confinement (Mayor et al., 2023).

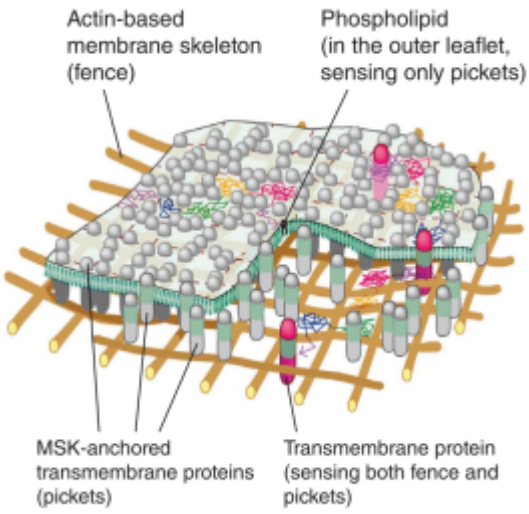

Fig. 2: Illustration of the Anchored-Picket Fence Model depicting the corralling of membrane components into domains fenced by the actin cytoskeleton and picketed by transmembrane proteins anchored to the cytoskeleton (adapted from Mayor et al., 2023).

Active-Composite Model

All of the models discussed thus far assume that membrane components are passively organised by equilibrium processes emerging from protein-protein, lipid-lipid and lipid-protein interaction (Rao and Mayor., 2014). However, we know that energy-consuming non-equilibrium processes are characteristic of all living systems. Active processes that remodel the membrane include endocytosis, exocytosis, as well as energy-consuming flippases (Mayor et al., 2023). Beyond this, the membrane is closely associated with a dynamic actin cortex that undergoes ATP-dependent treadmilling as well as contractility by myosins.

The Active Composite model views the cell surface as a composite of a multicomponent plasma membrane intimately linked with a multicomponent dynamic actin cortex. It predicts that membrane components bound to the actin cortex can experience transient clustering due to contractile stresses and currents generated by myosin activity on short, dynamic actin filaments (Rao and Mayor, 2014; Gowrishankar et al., 2012). These short filaments spontaneously assemble into contractile platforms called ‘asters’ due to stochastic processes, including actin treadmilling, filament crosslinking and motor activity of myosin. Membrane components transiently linked to such filaments directly or indirectly undergo advection towards the centre of asters, resulting in their transient nano-clustering (Gowrishankar et al., 2012; Kalapurakkal et al., 2020) (Fig. 3). The model predicts that all actin-binding membrane components are capable of experiencing clustering due to actomyosin activity (Gowrishankar et al., 2012). It categorises membrane components into inert, passive and active based on the nature of their association with the dynamic actin cortex (Rao and Mayor, 2004). Inert components don’t bind with actin filaments and hence are inert to actomyosin contractility (e.g. lipids having unsaturated acyl chains). Passive components can bind with actin filaments and undergo clustering (GPI-anchored proteins, Ras proteins). Active components, on the other hand, not only bind actin filaments but can also remodel the actin cortex (e.g. formin, Arp2/3, and integrin receptors) (Mayor et al., 2023).

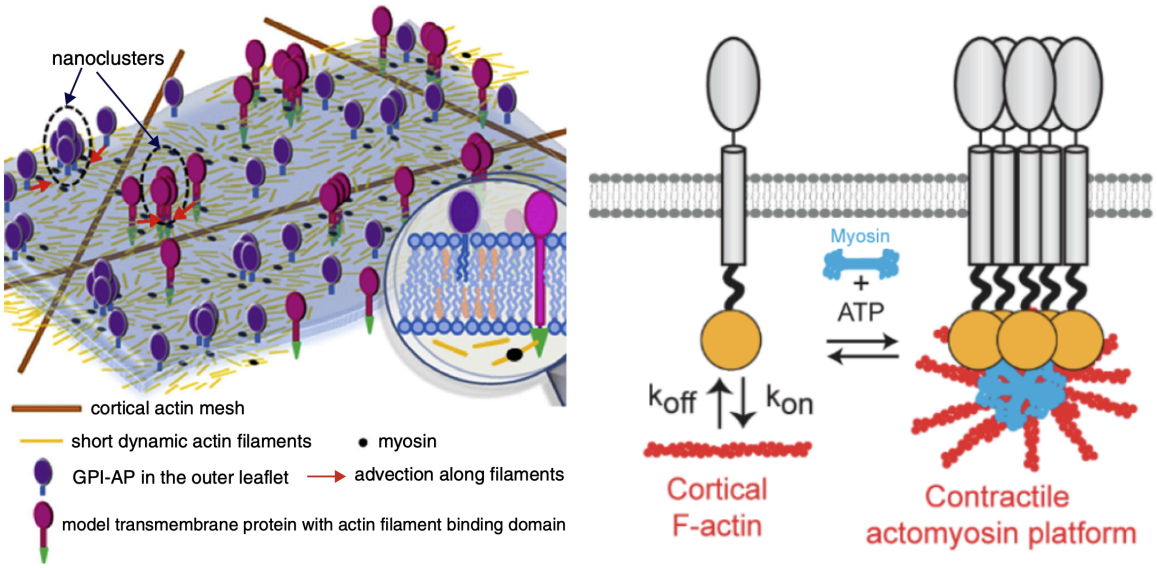

Fig. 3: Illustration of the Active Composite model. The model suggests that membrane components that bind actin filaments can undergo transient clustering due to contractile stresses generated by myosin motor activity on short dynamic actin filaments (adapted from Rao and Mayor, 2014 and Bhat, 2023).

The Active Composite model emerged as a way to understand the non-equilibrium dynamics of certain proteins, like outer leaflet GPI-anchored proteins and inner leaflet Ras proteins, that are inconsistent with prevailing interpretations of a passively organised, equilibrated plasma membrane (Sharma et al., 2004; Goswami et al., 2008; Rao and Mayor, 2014). These proteins show anomalous density fluctuations, forming transient nano-clusters whose formation and fragmentation are independent of temperature and concentration and are sensitive to ATP-consuming actomyosin activity (Sharma et al., 2004; Plowman et al., 2005; Goswami et al., 2008; Saha et al., 2015; Raghupathy et al., 2015). These clusters disappear when the membrane is detached from the cytoskeleton, and their formation/fragmentation dynamics are inhibited when myosin activity is inhibited by blebbistatin (Goswami et al., 2008). The formation of these clusters is necessary for the signalling and sorting functions of these proteins (Sharma et al., 2004; Plowman et al., 2005; van Zanten et al., 2009; Kalapurakkal et al., 2019). Nanoclusters exhibit trans-bilayer coupling with the actin cortex (Raghupathy et al., 2015) and may be crosslinked to generate larger mesoscale assemblies (Goswami et al., 2008; van Zanten et al., 2009; Sengupta et al., 2011).

The Active Composite model doesn't preclude or disqualify the anchored-picket fence model or the formation of nano-scale Lo-like domains. Rather, it describes an additional mechanism that can help generate functional heterogeneities on the membrane. An integrated view of membrane organisation would look at nano and mesoscale heterogeneities occurring at different levels: i. Corralling by actin fences and pickets, ii. Clustering due to passive protein-protein interactions between protein monomers, iii. Partitioning of components into nano-scale domains generated by spontaneous lipid-lipid demixing, and iv. Active clustering due to binding with the actomyosin cortex.

In Vitro Reconstitution of Active Composites

Koster et al., 2016 created a step-wise assembly of a supported lipid bilayer containing an EzrinABD membrane-actin linker, followed by pre-polymerised actin filaments and skeletal muscle myosin II filaments (Fig. 4). They varied actin and myosin concentrations as well as actin filament length (by varying capping protein concentrations) and observed distinct states of actomyosin configurations, including the formation of asters by shorter, polar actin filaments. They observed that EzrinABD membrane-actin linker proteins could be clustered by these polar actomyosin asters. These clusters showed hallmarks of active dynamics, including anomalous density fluctuations.

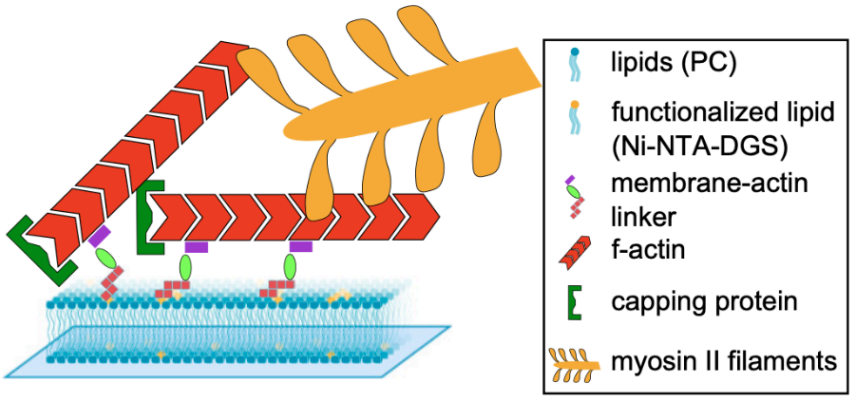

Fig. 4: Schematic of the *in vitro* reconstitution set-up developed by Koster et al., 2016 and 2022 (adapted from Koster et al., 2016).

The *in vitro* approach allowed for the reconstitution of the minimal set of ingredients required to recapitulate the actomyosin-dependent clustering of membrane components and to characterise this behaviour through quantitative imaging. However, the work was limited by the nature and length scales of actin filaments that could be generated, as well as the choice of myosin used.

A key assumption of the Active Composite model is the existence of a distribution of shorter dynamic actin filaments of the range 0.1 to 0.3 μm that are produced by continuous treadmilling (Gowrishankar et al., 2012). Using capping proteins, Koster et al., 2016 were able to generate asters using stable pre-polymerised actin filaments of length 2-7 μm.

Koster et al., 2016 also opted for skeletal muscle myosin II, which is specialised for muscle contraction in skeletal and cardiac muscle cells, rather than non-muscle myosin II, which is found across ubiquitously eukaryotic cell types. Non-muscle myosin II is involved in diverse cellular processes that require cytoplasmic actin contractility, such as cell division, motility, adhesion, mechanotransduction and differentiation (Vincente-Manzanares et al., 2009; Quintanilla et al., 2023). The two proteins also differ in their size, length scale, and motor activity kinetics. Koster et al., 2016 generated myofilaments of length 0.5 to 1.2 μm using skeletal muscle myosin II. However, non-muscle myosin II filaments *in vivo* are usually 0.2-0.3 μm in length (Vincente-Manzanares et al., 2009). Skeletal muscle myosin II is reported to have a motor activity of 5-6 $\mu m^2/s$ while non-muscle myosin II is reported to have a motor activity of 0.1-3 $\mu m^2/s$ (Thoresten et al., 2013; Stam et al., 2015). Thus, non-muscle myosin II would be the more physiologically relevant myosin to test in an *in vitro* reconstitution set-up in conjunction with spontaneously polymerising actin filaments to verify the predictions of the Active Composite model.

Dynamic Actin Cortex

The actin cytoskeleton is home to over 150 different actin-binding proteins. Formins and Arp2/3 nucleate linear and branched actin filaments, respectively. Profilin binds G-actin

monomers and promotes actin filament polymerisation. Capping proteins limit actin filament length, and cofilin severs actin filaments. Myosin 1 motors and members of the ezrin-radixin-moesin family physically link the actin cortex to the plasma membrane. In cells, the substrate for actin filament polymerisation is G-actin complexed with profilin. Formin is thought to nucleate filament assembly by binding the growing barbed end of the actin filament on its FH2 domain and recruiting G-actin-profilin by its FH1 domain (Breitsprecher et al., 2013; Chugh et al., 2018). In order to reconstitute a minimal dynamic actin cortex *in vitro*, the following ingredients are required: G-actin, profilin, formin and a membrane-actin linker. Additional control over the length of filaments can be provided by cofilin and capping proteins.

In vitro, G-actin monomers are maintained in monomeric form in the absence of K^+ and Mg^{2+} and can polymerise in the presence of these ions (Pardee and Spudich, 1982). Above a critical concentration of 100 nM, G-actin monomers can spontaneously nucleate to form actin filaments in the absence of other proteins like formin and profilin (Pollard et al., 2016). Koster et al., 2016 reconstituted stable pre-polymerised actin filaments over a supported lipid bilayer. These filaments had been spontaneously nucleated above the critical concentration in the absence of profilin and formin, and allowed to polymerise before addition to the bilayer. Filaments of varying lengths were generated using varying concentrations of capping protein and tethered to the bilayer using an EzrinABD membrane-actin linker.

Non-muscle myosin II

Non-muscle myosin II (NMII) is a hexameric protein consisting of three pairs of polypeptides: a pair of heavy chains (HC) that wrap around each other in a coiled-coil fashion, along with two pairs of light chains: the essential light chain (ELC) and the regulatory light chain (RLC) (Fig. 5). The heavy chains consist of three domains: an N-terminal head, a neck and a C-terminal tail. The head domain is the catalytic domain, containing binding sites for actin and ATP. The neck domain contains binding sites for the two pairs of light chains. The tail domain allows the pair of heavy chains to wrap around one another and enables myosin proteins to self-assemble into bipolar filaments

consisting of ~30 NMII monomers. These bipolar filaments can bind and crosslink actin filaments in an anti-parallel fashion. The head domains can walk along actin filaments using energy obtained from ATP hydrolysis (Vincente-Manzanares et al., 2009). The movement of the head domain is amplified by the neck domain, which acts as a lever to generate a power stroke that translocates actin filaments relative to the myosin molecule, resulting in the sliding of filaments and generation of tension (Sellers and Heissler, 2019).

The activity of non-muscle myosin II is regulated by the reversible phosphorylation of the regulatory light chain by a variety of kinases, including myosin light chain kinase (MLCK). Phosphorylation significantly promotes the ATPase activity of the head domain on binding to F-actin. Phosphorylation is also suspected to bring about a conformational change from a closed, assembly-incompetent structure to an open structure that allows for self-assembly into filaments (Vicente-Manzanares et al., 2009; Quintanilla et al., 2023).

Vertebrates produce three isoforms of NMII: NMIIA, NMIIB, and NMIIC, the identities of which are determined by the heavy chain isoform present: NMIIA-HC, NMIIB-HC, and NMIIC-HC (Sellers and Heissler, 2019). The light chains are common to all isoforms. NMIIA and NMIIB are the most dominant of the three and are produced in the greatest quantities. Among the three, NMIIA has the highest ATPase rate and highest motor activity, while NMIIB has the highest duty ratio (Kovacs et al., 2003; Wang et al., 2003).

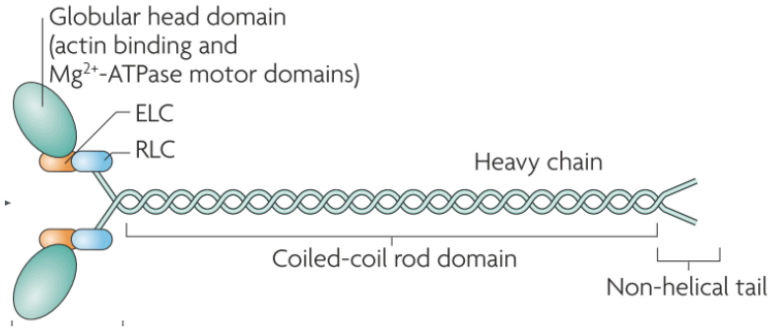

Fig. 5: Structure of non-muscle myosin II (adapted from Vincente-Manzanares et al., 2009).

Bac-to-Bac Expression System

The Bac-to-Bac™ baculovirus expression system makes use of site-specific transposition to generate recombinant baculoviruses, which can be used to infect *Spodoptera frugiperda* Sf9 insect cells to express recombinant proteins (Fig. 6). A mini-Tn7 transposon is used to shuttle desired genes from a donor vector onto a Tn7-*att* target site on a baculovirus circular genome or 'bacmid' present inside DH10Bac *E. coli* cells (Fig. 6). The transposition is facilitated by a transposase encoded by a helper plasmid also present in the DH10Bac *E. coli* cells. Successful transposition onto the Tn7-*att* target site leads to the disruption of *lacZ* alpha-complementation on the bacmid, allowing for blue-white screening of recombinants. Recombinant bacmids thus generated can be introduced into Sf9 cells to generate recombinant baculoviruses. These viruses carry the recombinant gene with them as they infect new cells, prompting the cells to express the desired recombinant proteins.

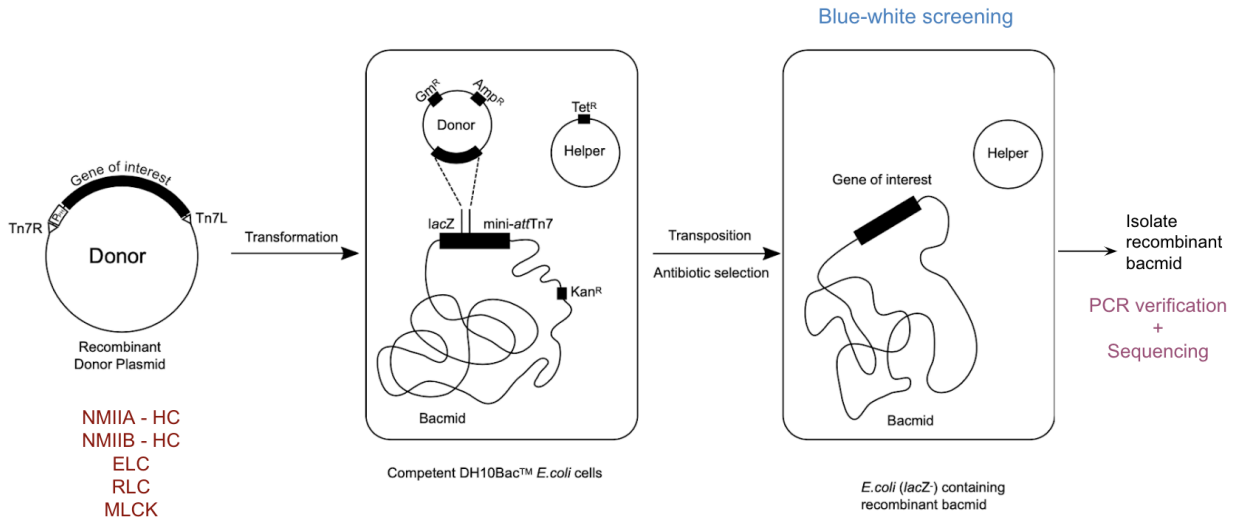

Fig. 6: Schematic describing how recombinant bacmids are generated using the Bac-to-Bac™ expression system (adapted from the Bac-to-Bac™ Baculovirus Expression System User Guide, Gibco)

Chapter II: Aims and Objectives

The broader aim of this thesis is to build a minimal actomyosin cortex over a supported lipid bilayer *in vitro* from individual components. With this reconstitution set-up, the goal is to test whether non-muscle myosin II can cluster membrane components linked to short, dynamic actin filaments, as predicted by the Active Composite model. The essential components of this system are a freely diffusing supported lipid bilayer, purified non-muscle myosin II, as well as short, dynamic actin filaments. In this direction, the specific objectives of this thesis are as follows:

1. To recombinantly express and purify NMIIA and NMIIB isoforms of non-muscle myosin II along with myosin light chain kinase in Sf9 insect cells by baculovirus infection

2. To characterise the performance and limitations of the TIRF microscopy equipment

3. To create freely diffusing supported lipid bilayers

4. To reconstitute actin filaments of defined length using varying concentrations of capping protein

5. To create spontaneously polymerising dynamic actin filaments on a supported lipid bilayer using formin and profilin

6. Finally, to reconstitute purified and activated non-muscle myosin II with dynamic actin filaments over a supported lipid bilayer to test for the clustering of actin-membrane linker proteins due to actomyosin contractility

Chapter III: Materials and Methods

1. Constructs

pFastBac1™ donor vectors containing the following inserts: Flag-Halo-NMIIA-HC, Flag-Halo-NMIIB-HC, Flag-MLCK, ELC and RLC were received from Prof. James Sellers. The presence of these inserted regions was confirmed by Sanger sequencing using primers specific to the P_H promoter and SV40 Poly-A terminator regions flanking the insert.

Forward primer (P_H promoter): 5'- GGATTATTCATACCGTCCC - 3'
Reverse primer (SV40 poly-A): 5'- GATGAGTTTGGACAAACCAC - 3'

A recombinant bacmid and a P1 baculovirus stock encoding FLAG-Myosin 1c-EGFP had been previously generated by Bhagyashri Mahajan, NCBS.

2. Transformation of DH10Bac *E. coli*

50 µL of competent DH10Bac *E. coli* (Gibco) cells were incubated with 100 ng of the above-listed pFastBac1™ donor vectors in ice for 30 min. Heat shock was then performed by heating the cells with the donor vectors at 42°C for 45s, followed by immediate immersion in ice for 2 min. 900 µL of SOC Media (Gibco) was then added to the cells in 15 mL centrifuge tubes, and the cells were allowed to recover for 5 hours at 37°C in a shaker incubator. The cells were then plated in LB-Agar plates containing 50 µg/µL kanamycin, 10 µg/µL tetracycline, 7 µg/µL gentamicin, 120 µg/µL X-Gal, and 120 µg/µL IPTG. Single, large, separated, completely white (recombinant) and completely blue (negative control) colonies were selected from the plates following incubation for over 48 hours at 37°C. The colonies were used to inoculate 10 mL of LB media containing the same antibiotic concentrations. Bacmids were isolated from these cultures after being grown overnight at 37°C in a shaker incubator.

3. Bacmid Isolation

The overnight cultures were spun down at 6,000xg at 4°C for 15 min. The bacterial pellet was resuspended in P1 resuspension buffer, lysed using P2 lysis buffer, and treated with P3 neutralisation buffer (Qiagen) according to the manufacturer's instructions. The lysate was spun at 21,000xg at 4°C for 30 min to collect the supernatant. The bacmid DNA was then precipitated from the supernatant by chilling with a roughly equal volume of isopropyl alcohol overnight at -20°C. The precipitated DNA was pelleted from the mixture by spinning at 21,000xg at 4°C for over 30 min. It was then washed in 800 µL of 70% ethanol by partial resuspension followed by spinning down at 21,000xg at 4°C for at least 15 min. The supernatant was discarded, and the DNA pellet was air-dried to remove any residual ethanol before being resuspended in 55°C hot nuclease-free water. The isolated bacmid DNA was stored at -20°C.

PCR was performed to confirm that the bacmids isolated from white colonies were recombinant by using M13 primers specific to sites that flank the Tn7-*att* site on the bacmid.

Forward primer: 5' - GTAAAACGACGGCCAGT - 3'
Reverse primer: 5' - CAGGAAACAGCTATGAC - 3'

The PCR products were run on a 1% agarose gel and imaged on an iBright imager (Thermo Fisher Scientific).

4. Cell Culture

Sf9 cells were maintained in suspension cultures at log phase at a density of 0.5 million to 2 million cells per mL in Sf-900™ II serum-free media (Gibco) at 27°C in a shaker incubator without any added antibiotics or antimycotics. In the log phase, cells doubled in density every 24 hours and were split to a density of 0.5 to 1 million cells per mL every two days. New flasks were seeded with cells at a density of 0.5 to 1 million per mL. Cells were allowed to adapt to new flasks for 2-3 days, and their health (cell density, viability and appearance) was monitored over a couple of passages before use

in any experiments. Only flasks containing healthy log phase cells that doubled in density every 24 hours and had a viability of ~90% or above (i.e. having ~10% or fewer dead cells) were used for experiments. Cell density was determined by counting the number of cells present in 10µL of culture using a hemocytometer. Cell viability was determined as the percentage of cells observed in a 1mm x 1mm grid of the hemocytometer that did not take up dye on staining with 0.4% trypan blue. Flasks were washed with 10% acetic acid and autoclaved twice (wet and dry cycle) before use.

5. Transfection of Sf9 Cells

Sf9 cells in the log phase had been split to a density of 1 million cells per mL the night before transfection. The following morning, 1 mL of these cells were seeded per well of a 6-well plate and allowed to adhere for 1 hour at 27°C. The transfection mix per well was generated by incubating 6 µL of Cellfectin II (Gibco) in 100 µL of SF900 II serum-free media (Gibco) for 10 min at room temperature. After which, 1 µg of isolated bacmid DNA diluted in 100 µL of media was added to the mix. The mix was then incubated for 1 hour at room temperature in the dark, following which an additional 800 µL of media was added. The transfection mix was finally added dropwise to the adherent cells, which were then incubated at 27°C for 5 hours, after which the media containing the transfection mix was aspirated and replaced by 2 mL of fresh media. The cells were then allowed to incubate at 27°C for over 5 days until a good transfection efficiency was achieved. The cells and media were then collected and spun down at 1,000xg at 4°C for 10 min. The supernatant was preserved as the P0 stock of baculoviruses and stored at 4°C in the dark. A bacmid encoding Myosin 1C-EGFP was used as a positive control for transfection to monitor transfection efficiency.

6. Amplifying P0 baculovirus stock

40 mL cultures of Sf9 cells in log phase were infected with 0.1% to 3% (v/v) of P0 baculovirus stocks after being split to a density of 1 million cells per mL and were allowed to grow at 27°C in a shaker incubator. The density and viability of the cells were tracked for over 5-7 days until only 10% of the cells were viable. The culture was then collected and spun down at 3,000xg at 4° for 15 min. The supernatant was preserved as

the P1 stock of baculoviruses and stored at 4°C in the dark. A WT uninfected flask was maintained as a negative control for infection to compare cell densities and viabilities.

7. Lysate Preparation

40 mL cultures of Sf9 cells in the log phase were infected with 1% to 2% (v/v) of P1 stocks of baculoviruses after being split to a density of 1 million cells per mL. The cells were allowed to grow at 27°C in a shaker incubator until they reached 80% cell viability. The culture was then pelleted at 3,000xg at 4°C for 15 min. Cell pellets were flash-frozen in liquid nitrogen and stored at -80°C until the time of lysate preparation. The cell pellets were thawed in 200 µL of lysis buffer in ice and were lysed using 10-15 strokes of a Dounce's homogeniser. The homogeniser was thoroughly rinsed with Milli-Q water and 70% ethanol before use. The lysate was spun down at 21,000xg for over 20 min at 4°C until the supernatant was clarified. The concentrations of the whole lysate, the pellet and the supernatant fractions were determined by BCA assay. The fractions were heated for 5 min 30s at 95°C in 1x Laemmeli buffer to make samples for SDS Page. These samples were stored at -20°C.

8. Western Blot for Protein Expression

SDS Page samples of the whole lysate, pellet and supernatant fractions were resolved on a 10% SDS polyacrylamide gel. 100 µg of the whole lysate, pellet and supernatant fractions and 1 µg of purified control protein were loaded. The resolved proteins were transferred onto an activated PVDF membrane by wet transfer using Tris-Glycine buffer containing 20% methanol and 0.01% SDS. The membrane was blocked in 5% BSA in 1x Tris-buffered saline (BioRad) supplemented with 0.1% Tween-20 (TBST) for 1.5 hours, then incubated with mouse anti-FLAG M2 primary antibodies (Sigma Aldrich) overnight at 4°C, washed with TBST and then incubated with HRP-conjugated anti-mouse secondary antibodies for 1.5 hours. Incubation with antibodies was done under gentle rocking in 3% BSA in TBST at the recommended dilution (1:1000 for the primary and 1:5000 for the secondary antibody). The blot was then rinsed with TBST buffer before being developed with Super Signal WestPico chemiluminescent substrate (Thermo Fisher Scientific) and imaged on an iBright imager (Thermo Fisher Scientific).

9. MLV and SUV preparation

A lipid mix containing 98 mol% DOPC and 2 mol% DGS-NTA (Ni) (Avanti) was prepared in chloroform in amber vials using Hamilton syringes. The chloroform was evaporated from the vial under a slow nitrogen gas stream followed by vacuum desiccation at room temperature for over 2 hours. The desiccated lipid mix was then resuspended in the lipid rehydration buffer to achieve a final lipid concentration of 4 mM. The resuspension was vortexed for 30s to generate MLVs. 250 µL aliquots of the MLVs were flash-frozen in liquid nitrogen and stored at -20°C for up to 6 weeks (Koster et al., 2022).

The MLV aliquots were later thawed at room temperature and subjected to 10-15 freeze-thaw cycles by plunging in liquid nitrogen for 30s followed by 2 min in a water bath maintained at 42°C. Next, the aliquot was subjected to 2-3 rounds of microtip sonication (ON time = 15s, OFF time = 30s) at 30% amplitude until the solution became clear. The microtip sonicator was washed with 2.5M KOH, followed by chloroform and Milli-Q water before use. Following sonication, the aliquot was centrifuged at 15,000xg for 45-60 min at 4°C, and the top 60% of the solution containing SUVs was collected and stored in ice at 4°C for up to 7 days (Koster et al., 2022).

10. Sample chamber preparation

22mm x 40 mm number 1 thickness glass coverslips (Epredia) were washed with 2% Hellmanex III cleaning solution at 65°C for 40 min in a Coplin jar in a bath sonicator (GT Sonic) at ‘normal’ pulse mode. The coverslips were then rinsed thoroughly with Milli-Q water. Next, the coverslips were washed with 2.5M KOH in a Coplin jar for 7 min in a bath sonicator at ‘normal’ pulse mode. The coverslips were then rinsed thoroughly again with Milli-Q water before being blown dry under a stream of nitrogen gas. To make sample chambers, the lids and bottom halves of 0.5 mL PCR tubes were cut off using a pair of scissors and a sharp blade. UV curable glue (Norland Optical Adhesive 88) was applied to the rim of the top half of the cut PCR tubes, which were then stuck upside-down onto clean coverslips. The glue was cured by subjecting coverslips to 15 min of UV light (PSD-UV8T; Novascan) (Koster et al., 2022).

11. Supported lipid bilayer preparation

The sample chambers were first washed 3 times with PBS, leaving 100 µL of the buffer behind. The level of the buffer was marked using a permanent marker to track changes in buffer volume. The level of buffer in the chamber was brought back to the 100 µL level marking after each wash during this procedure. First, 3 µL of 0.1 M $CaCl_2$ was added to the chamber, followed by 5 µL of the SUV solution. After gentle mixing with a micropipette, the SUVs were allowed to adsorb to the coverslip for 15 min to form the supported lipid bilayer. Then, the chamber was washed 10 times with KMEH buffer (by adding 100 µL of KMEH buffer, mixing gently, and removing 100 µL each time) in order to remove any unbound SUVs. Then, 5 µL of 1 mg/mL β-casein was added to the chamber and allowed to incubate for 10 min before being washed 3 times with KMEH. Then, Alexa Fluor 488 labelled 10xHis-Snap-UtrophinABD was added to the chamber at a final concentration of 20 nM and incubated for 20 min before being washed 3 times with KMEH (Koster et al., 2022). In experiments with formin, 10 nM of Alexa Flour 488 labelled 10xHis-Snap-UtrophinABD was added to the chamber along with 10 nM of 6xHis-Cdc12 (formin) and allowed to incubate for 20 min before being washed 2 times with KMEH (Palani et al., 2021).

12. Creating the actin meshwork

For experiments with pre-polymerised actin, an actin Polymerisation Mixture consisting of 1 volume of G-actin, 1 volume of CapZ, and 2 volumes of 2x Target Buffer was created. The G-actin component contained 20 µM of G-actin (10% labelled with Atto 561) along with 10% of 10x ME buffer in G-buffer. The CapZ component contained 4 times the desired concentration of CapZ diluted in G-buffer. If no CapZ was used, then just 1 volume of G-buffer was added to the G-actin component. Finally, 2 volumes of 2x Target Buffer were added to this, bringing the final actin concentration in the Polymerisation Mixture to 5 µM, the final CapZ concentration to the desired concentration, and the Target Buffer concentration to 1x. After adding the Target Buffer, the Polymerisation Mixture was mixed gently only 1-2 times with cut blunt-end tips to minimise shear. The Polymerisation Mixture was incubated at room temperature in the dark for 45 - 60 min to allow the actin to polymerise. After this, the polymerised actin

was kept in ice until it was to be added to the chamber. Cut blunt-end tips were also used to transfer the desired amount of the pre-polymerised F-actin to the chamber. It was mixed gently with the buffer present in the chamber 1-2 times using a cut blunt-end tip to minimise shear (Koster et al., 2022).

In experiments with formin and profilin, a mixture containing 4 μM of G-actin (20% labelled with Atto 565) along with 5 μM of 6xHis-Sumo-Cdc3 (profilin) and 10% of 10x ME buffer in G-buffer was created. The mixture was incubated in ice for 5 min before it was added to the chamber to achieve the desired final concentration of G-actin-profilin (Palani et al., 2021).

13. Characterising Nikon TIRF properties

A Nikon Ti Eclipse microscope equipped with a TIRF unit, a Perfect Focus System and an sCMOS camera (Photometrics 95b) was used. A Laser combiner (Agilent MLC 400) and LED (CooLED) were used as light sources. An optical power meter (ThorLabs) was used to measure the illumination power at the back focal plane. Images were captured using MicroManager, and images were analysed in Fiji. Images were taken using a 20x, 0.75 NA objective with LED 488 nm illumination on an autofluorescent plastic slide (Chroma) for the camera gain value calibration, linearity and stability experiments. The camera gain values for each pixel of the sCMOS camera were computed as the slope of the linear regression of variance in signal plotted against the mean signal at a fixed exposure time and different LED illumination powers (Lambert and Waters, 2014). Mean signal intensity was measured at a fixed exposure time and LED power for the camera stability measurement and at a fixed LED power but varying exposure times for the linearity experiment. The XY resolution of a 100x, 1.45 NA objective was determined manually by computing the full-width half maximum distance of the Z intensity profile of 100 nm TetraSpeck beads (Invitrogen) mounted on a glass slide illuminated by a 488 nm laser. When coupled with a 1.5x tube lens, the 100x 1.45 NA objective yielded a pixel size of 73.3 nm.

14. TIRF microscopy for the supported lipid bilayer and actin

The supported lipid bilayer and actin meshwork were imaged with the 100x, 1.45 NA oil immersion objective in TIRF using the 488 and 561 nm lasers with a 1.5x tube lens. Typically, a set laser power of 5-20, along with an exposure time of 100 to 200ms, was used for all image acquisitions, with the ND filters and polarisers in the path. During FRAP experiments, the image acquisition was first paused manually. Then, the field diaphragm was closed and the laser power was increased to its maximum value for 5-10s to bleach the fluorophores on the supported lipid bilayer. Finally, the field diaphragm was opened, the laser power was reduced to its original value, and the image acquisition was resumed. Images were taken at an interval of 2s for a period of 5 min for FRAP experiments. Images of actin polymerisation were taken every 1 or 2s for a duration of 5 min.

13. Analysis

Data fitting was performed on Prism GraphPad and MATLAB. Graphs were plotted on Prism GraphPad or Google Sheets.

<u>FRAP:</u>

After background subtraction, a circular ROI was selected over the bleach spot, and the mean intensity in the ROI was computed for each frame before and after the photobleaching. A reference ROI of the same area was selected over a different unbleached portion of the supported lipid bilayer in the same field, and its mean intensity was computed for each frame. The FRAP trace was then generated by normalising the mean intensity over the bleach spot by the mean intensity in the reference spot in order to account for the photobleaching experienced by the whole field over the course of the entire image acquisition. The FRAP trace was then fit to an exponential fit model (Kang et al., 2012):

$$f(t) = A + B\,(1 - e^{-Ct})$$

The half-time of the recovery is computed using the exponential decay constant, C, as:

$$T_{1/2} = 0.693/C$$

A line scan through the centre of the bleach spot was used to obtain an intensity profile of the bleach spot. This intensity profile was normalised to the intensity profile of the same line prior to the bleaching event. The normalised intensity profile thus obtained was fit to a Gaussian fit model (Kang et al., 2009):

$$f(x) = \exp(-K \exp(-2(x-a)^2/R^2)$$

Where R is the effective bleach radius. The diffusion coefficient was then computed using the effective bleach radius and half-time of recovery as (Axelrod et al., 1976, Koster et al., 2016):

$$D = 0.88R^2 /4T_{1/2}$$

Filament Length and Elongation Rate:

Filament length was calculated manually using the segmented line tool in Fiji. ROIs of 25 µm x 25 µm were selected, and all filaments in the ROI were measured. Elongation rates were measured as the slope of kymographs of elongating actin filaments. Kymographs were generated manually using the Multi Kymograph tool in Fiji. The slope of the kymograph was computed manually using the angle tool. The slope in pixel/pixel was converted to an elongation speed in µm/s by multiplying the former by the pixel size (0.0733 µm) and dividing it by the frame interval (1 or 2s). The elongation speed was then converted to an elongation rate in actin subunits per second by assuming 370 actin subunits are present per µm of an actin filament (Pollard et al., 2000). Actin filament elongation rate was measured from movies captured immediately after the addition of the actin-profilin mix to the supported lipid bilayer.

14. Protein Purification

Chicken breast actin and 10xHis-Snap-UtrophinABD had been previously purified and labelled by Bhagyashri Mahajan and Sankarshan Talluri, NCBS, as per previous reports (Pardee and Spudich, 1982; Spudich and Watt, 1971; Bhat, 2023). Mouse CapZ had also been previously purified by Bhagyashri Mahajan and Sankarshan Talluri, NCBS, as per previous reports (Funk et al., 2021; Koster et al., 2016).

The purified actin was labelled with maleimide-Atto-565 (Atto-Tec GmbH) and maintained in monomeric form in ice in G-buffer. The concentration and degree of labelling of labelled actin were measured by spectrophotometry (Implen NanoPhotometer) using the corrected absorbance at 290 nm for actin and the absorbance at 564 nm for the dye.

$$[\text{Unlabelled actin}] = A_{290} / \varepsilon_{290}$$

$$[\text{Labelled actin}] = [A_{290} - (A_{564} * cf)] / \varepsilon_{\text{actin, 290}}$$

$$[\text{dye}] = A_{564} / \varepsilon_{\text{dye, 564}}$$

$$\text{Degree of labelling} = [\text{dye}]/[\text{labelled actin}]$$

Where the molar extinction coefficient of actin at 290 nm (ε_{290}) is 26,600 M^{-1} cm^{-1}, the molar extinction coefficient of Atto-565 dye at 564 nm ($\varepsilon_{\text{dye, 564}}$) is 1.2 x 105 M^{-1} $cm^{-1,}$ and the correction factor (cf) for Atto 565 at 280 nm is 0.12.

10xHis-Snap-UtrophinABD was labelled with Alexa fluor 488. CapZ was unlabelled, and its concentration was measured by its absorbance at 280 nm (ε_{280}: 99,530 M^{-1} cm^{-1}).

Saccharomyces pombe Formin 6xHis-Cdc12 (FH1-FH2; 740-1391) and *Saccharomyces pombe* Profilin 6xHis-Sumo-Cdc3 were received from Prof. Saravanan

Palani, IISc. They were purified from *E. coli* BL21(DE3) by Jayanti Kumar, IISc, as per previous reports (Saravanan et al., 2021).

FLAG-Myosin 1c-EGFP had been previously purified from Sf9 cells by Bhagyashri Mahajan, NCBS, via affinity chromatography, as per previous reports (Pyrpassopoulos et al., 2012).

15. Illustrations

Illustrations were made on BioRender.com

Name of Buffer	**Composition**
5x Laemmli buffer	0.25 M Tris, pH 6.8, 10% SDS, 50% Glycerol, 0.25% Bromophenol Blue. 0.5M DTT
Tris-Glycine Transfer Buffer	48 mM Tris, pH 8.8, 39 mM Glycine, 20% Methanol, 0.01% SDS
TBST	1x TBS (BioRad) with 0.1% Tween-20
Lysis buffer	50 mM MOPS, pH 7.0, 30 mM NaCl, 0.5 mM EGTA, 1% IGEPAL, 10% Glycerol, 1 mM DTT, 100 µg/µL PMSF and 1:100 dilution of Protease Inhibitor Cocktail (Calbiochem)
PBS	137 mM NaCl, 2.7 mM KCl, 10 mM Na_2HPO_4, 1.8 mM KH_2PO_4
KMEH	50 mM KCl, 1 mM $MgCl_2$, 1 mM EGTA, 20 mM HEPES
Lipid rehydration buffer	1x PBS, 5% sucrose
G-buffer	2 mM Tris, 0.1 mM $CaCl_2$, 0.2 mM ATP, 0.5 mM TCEP, 0.04% NaN_3, pH 8
ME buffer	50 mM $MgCl_2$, 0.2 mM EGTA, 10 mM HEPES, pH 7.2
2x Target Buffer	2 mg/mL BSA, 2 mM ATP stock, 40 mM DTT, 2x KMEH
100 mM ATP stock	100 mM ATP disodium salt hydrate, 50 mM Tris, pH 8, 50 mM NaCl, 5 mM $MgCl_2$, 2 mM EGTA

Table 1: Composition of buffers used

Chapter IV: Results

A. Recombinant Protein Expression in Sf9 Cells

1. Recombinant bacmids encoding MLCK, ELC, RLC, NMIIA-HC and NMIIB-HC were generated by site-specific transposition

Recombinant bacmids containing FLAG-tagged MLCK, NMIIA-HC, NMIIB-HC and untagged ELC and RLC genes were isolated from white DH10Bac *E. coli* colonies (*lacZ*-) following transformation with donor vectors and blue-white screening. The appearance of white colonies indicated that the transposition of the mini-Tn7 element onto the bacmid had been successful. The isolated bacmids were further validated by Sanger sequencing and PCR.

Sanger sequencing using primers specific to the P_H promoter and SV40 polyA terminator regions that flank the genes confirmed the presence of the 5' and 3' ends of the genes in both the donor vectors and the isolated bacmids (Fig. 7). PCR with M13 primers specific to regions that flank the Tn7-*att* target site on the bacmid confirmed the size of the transposed sequence in the bacmids (Fig. 7). Bands of the appropriate size were obtained for all bacmids when the PCR products were resolved on a 1% agarose gel (Fig. 8). An empty bacmid isolated from a blue colony (*lacZ*+) was used as a negative control for the PCR, while a bacmid that encodes a known gene (Myosin 1c-EGFP) was used as a positive control.

The expected band size from an empty bacmid is 0.3 kb, which corresponds to the distance between the annealing sites of the M13 primers (Fig. 7). The expected band size from recombinant bacmids corresponds to 0.3 kb + the length of the mini-Tn7 transposon, which in turn is 2kb + the length of the desired gene (Fig. 7).

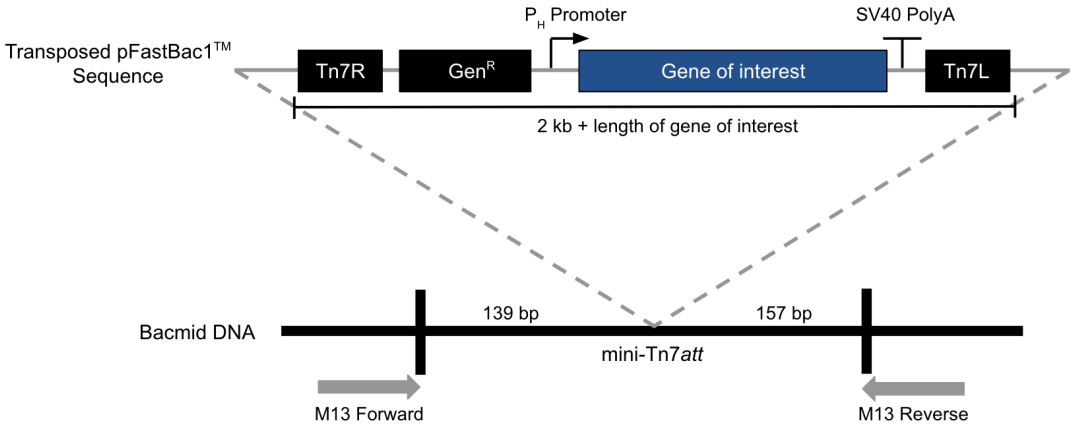

Fig. 7: Schematic of the transposition of the mini-Tn7 element from the pFastBac1 donor vector onto the bacmid. M13 forward and reverse primers anneal to sites flanking the Tn7-att site separated by 0.3 kb. The size of the mini-Tn7 transposon is 2 kb, excluding the length of the inserted gene (adapted from the Bac-to-Bac™ Baculovirus Expression System User Guide, Gibco).[16]

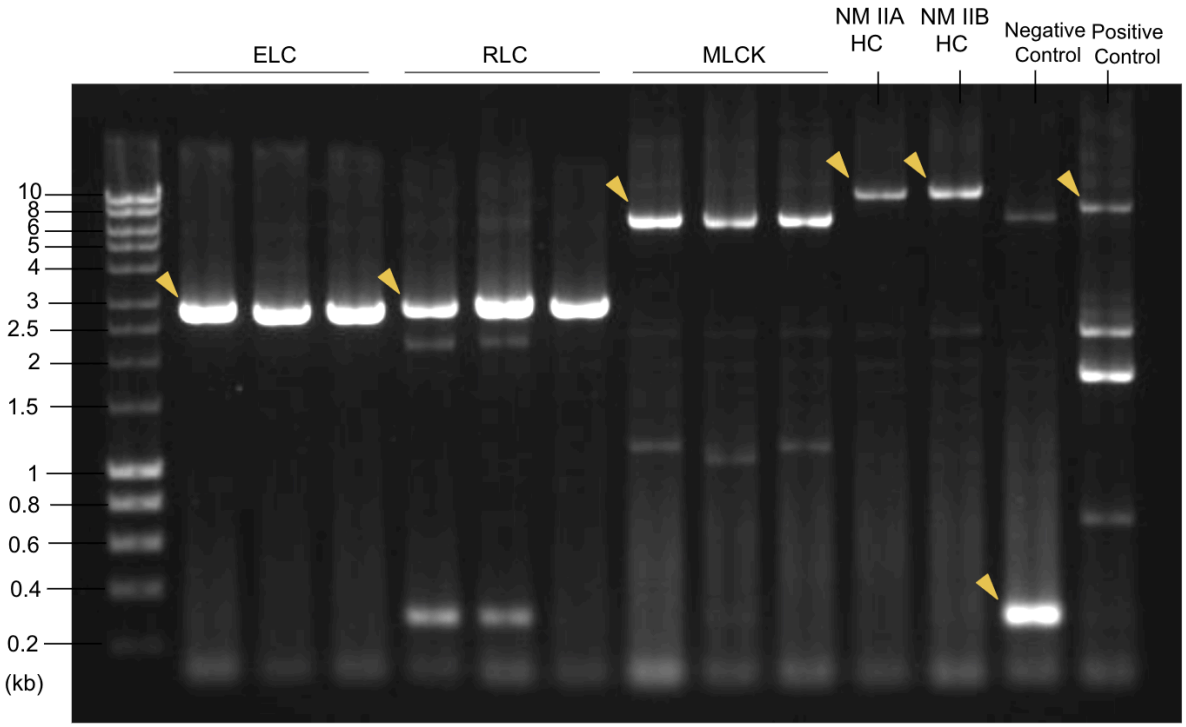

Fig. 8: PCR verification of presence and size of inserts in isolated bacmids following blue-white screening. A bacmid known to contain Myosin 1C-EGFP was used as a positive control, while an empty bacmid isolated from a blue colony was used as a negative control. Bands of interest are marked by a yellow arrow. Expected band sizes are as follows: ELC - 2.8kb, RLC - 2.8kb, MLCK - 5.5kb, NMIIA-HC - 9.7kb, NMIIB-HC - 9.8kb, negative control - 0.3kb, positive control - 7.1kb.

2. Transfection with MLCK, RLC and NMIIA-HC bacmids generated virulent baculovirus stocks

Sf9 cells were transfected with the recombinant bacmids to generate baculovirus stocks for all constructs (Fig. 9). A bacmid known to encode Myosin 1c-EGFP was used as a positive control for transfection (Fig. 10A). The P0 baculovirus stocks for all constructs were collected when maximum transfection efficiency (in terms of GFP-positive cells) was observed with the positive control bacmid.

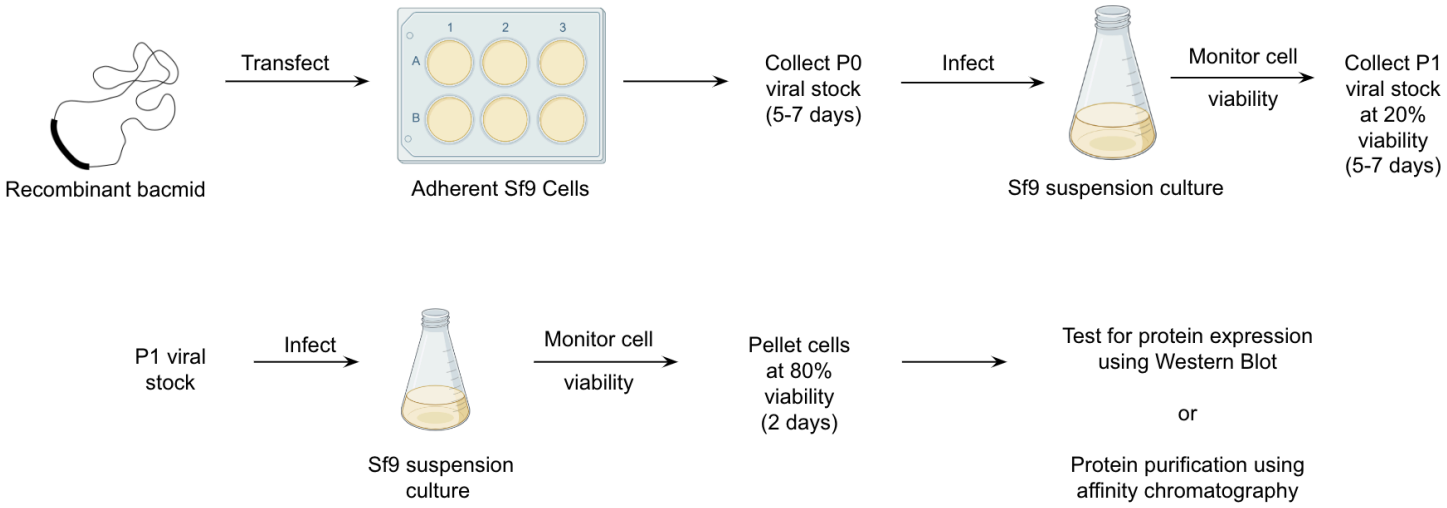

Fig. 9: Schematic representation of workflow to generate recombinant baculoviruses from bacmids to express proteins in Sf9 cells.

Sf9 cells were then infected with P0 baculovirus stocks to amplify the viral titre and generate P1 stocks (Fig. 9). The progress of the infection was monitored regularly by tracking the viability of infected cells through a Trypan-blue exclusion test. The viability of a WT uninfected culture was monitored as a negative control for infection. The viability of uninfected WT cultures of healthy, log-phase Sf9 cells is typically over 90% (i.e. under 10% of the cells are dead), while that of infected cells is expected to fall over the course of the infection. P1 stocks were collected when cell viability had fallen to ~10% (i.e. ~90% of cells were found dead).

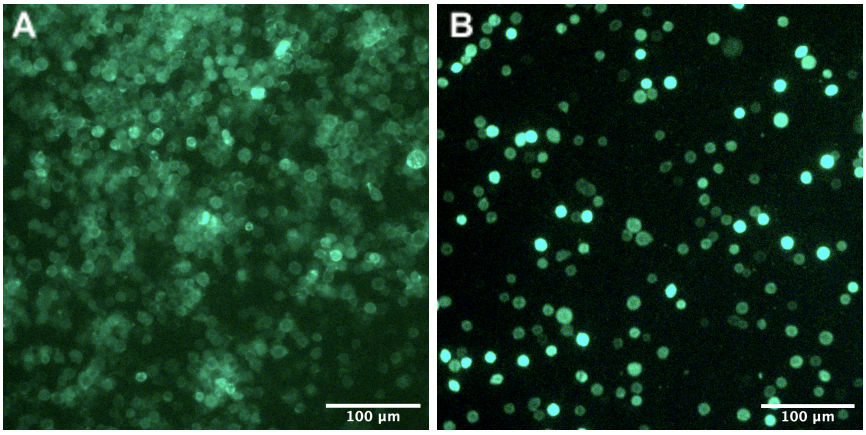

Fig. 10: GFP-positive Sf9 cells seen (A) on transfection with a control Myosin 1c-EGFP bacmid and (B) on infection with a control P1 stock of baculoviruses encoding Myosin 1c-EGFP

P1 baculovirus stocks of MLCK, RLC and NMIIA-HC were successfully generated, however, P1 stocks of ELC and NMIIB-HC could not be generated. Infection with 0.1% (v/v) concentrations of the P0 stocks of MLCK and RLC caused Sf9 cells to die as expected over the course of 5-6 days (Fig. 11A and 11B). Cells infected with 0.1% (v/v) of NMIIA-HC P0 took 9 days to reach 10% viability, suggesting the NMIIA-HC P0 might have had a comparatively lower viral titre.

When 0.1% (v/v) concentrations of the P0 stocks of ELC and NMIIB-HC were used to infect Sf9 cells, the cells didn't die as expected. The viability numbers remained stable at ≥90% and were comparable to those shown by a WT uninfected culture. The cells also showed no morphological signs of infection, such as an enlarged, granular or lysed appearance. The same result was obtained on infecting cells with 0.1% (v/v) concentration of P0 stocks generated from an alternate copy of the ELC bacmid that was isolated from another white DH10Bac *E. coli* colony.

Suspecting that the infection had been unsuccessful due to a low viral titre, the concentration of ELC and NMIIB-HC P0 stocks used was increased ten-fold to 1% (v/v). However, the cells still did not die as expected. They continued to show cell viability numbers that remained stable at ≥90%, again comparable to those shown by a WT uninfected culture (Fig. 11C). As a positive control for infection, Sf9 cells were also parallelly infected with a 1% (v/v) of a previously generated P1 baculovirus stock known

to encode Myosin 1c-EGFP. GFP-positive cells were seen on the infection (Fig. 10B), and the infected cells died as expected over 6 days (Fig. 11C).

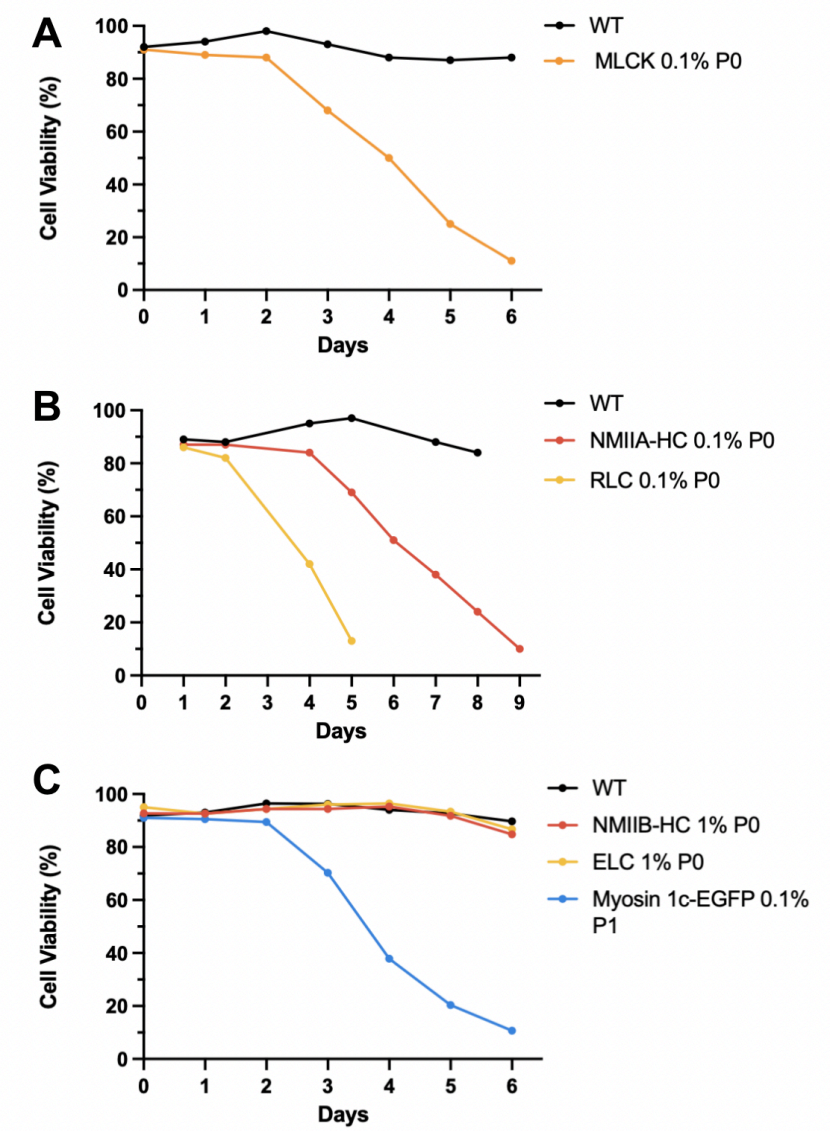

Fig. 11: Cell Viability measurements taken during the generation of P1 baculovirus stocks of (A) MLCK, (B) RLC, NMIIA-HC, (C) ELC, and NMIIB-HC. WT uninfected cells were monitored as a negative control. Baculoviruses were added to the cultures on Day 0. Cell viability was determined by the Trypan Blue exclusion test. 100-500 cells were counted per time point.

Thus, the P0 stocks generated from the ELC and NMIIB-HC bacmids were not virulent, indicating that perhaps transfection with the ELC and NMIIB-HC bacmids may have been unsuccessful in generating viruses. Consequently, transfection with the ELC and NMIIB-HC bacmids was repeated with a higher concentration of bacmid DNA (3 µg, rather than 1 µg used in the previous attempt). The newly generated ELC and NMIIB-HC P0 stocks were then used to infect Sf9 cells at 3% (v/v) concentration. Still, the cells showed no signs of infection or decrease in viability numbers, suggesting that perhaps the isolated ELC and NMIIB-HC bacmids are unable to code for infectious baculovirus particles. Possible reasons for this might be mutations in some essential viral genes or degradation of the bacmid DNA.

3. MLCK and NMIIA-HC expression was detected in Sf9 cells

Lysates generated from Sf9 cells infected with 2% (v/v) concentration of P1 stocks of MLCK or NMIIA-HC were probed for protein expression by western blot using anti-FLAG antibodies. Full-length FLAG-tagged MLCK protein (predicted size of 128 kDa) was detected in the whole lysate, as well as the supernatant fraction of the spun-down lysate generated from infected cells. Most of the protein was extracted into the soluble supernatant fraction during lysis, which is favourable for the purification of the protein (Fig. 12A). Additionally, numerous degradation bands of FLAG-NMIIA-HC were detected in the whole lysate generated from infected cells (Fig. 12B). While a protein band was seen at a higher molecular weight in the NMIIA-HC lysate than the 225 kDa band in the ladder, it is difficult to confirm whether it corresponds to the full-length protein (297 kDa). The detection of degradation bands of NMIIA-HC is anticipated as it was expressed in the absence of its light chains, which is required for its stable expression.

A lysate generated from WT uninfected cells was used as a negative control. Previously purified FLAG-Myosin 1c-EGFP or lysates generated from cells infected with 1% (v/v) of a previously generated P1 stock of baculoviruses known to encode FLAG-Mysoin 1c-EGFP were used as positive controls.

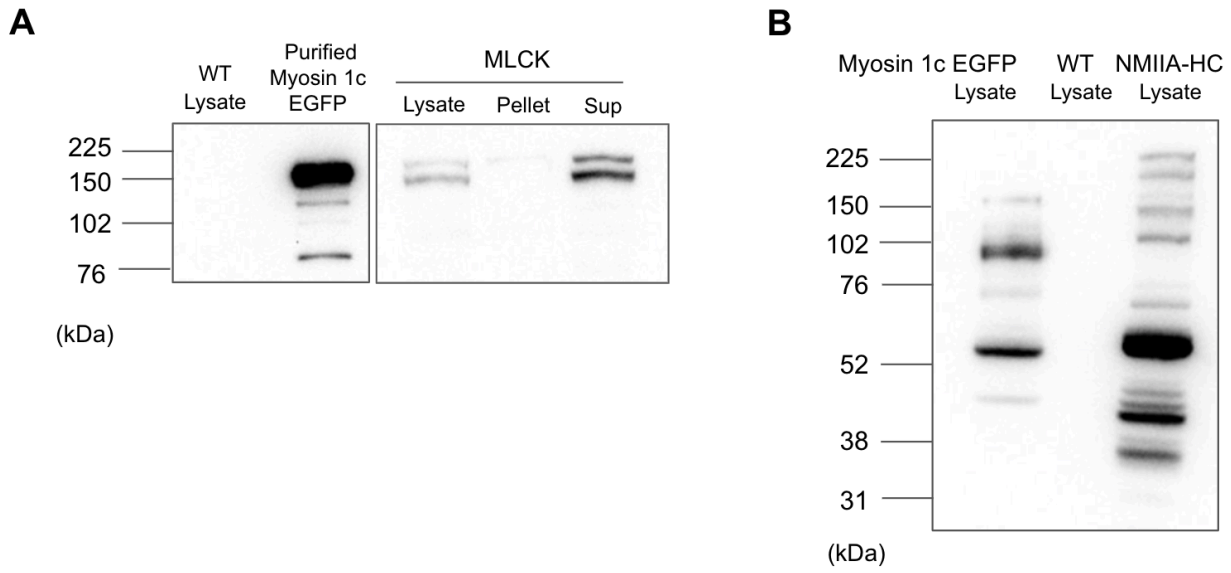

Fig. 12: Western blots probing for FLAG-tagged (A) MLCK and (B) NMIIA-HC expression using anti-FLAG antibodies. WT uninfected cells were used as a negative control. Purified FLAG-Myosin 1c-EGFP or lysate of cells infected with FLAG-Myosin 1c-EGFP encoding baculoviruses were used as a positive control. Expected band sizes are as follows: FLAG-MLCK: 128 kDa, FLAG-NMIIA-HC: 297 kDa, FLAG-Myosin 1c-EGFP: 147 kDa. Lysate: Whole lysate, Pellet: Pellet fraction of spun-down lysate, Sup: Supernatant fraction of spun-down lysate. Blots were cropped to show the relevant lanes.

B. Characterising properties of TIRF microscope for quantitative imaging

Various parameters of the TIRF microscope, camera and light sources were characterised to assess the performance and limitations of these instruments and to aid with quantitative image analysis.

1. Illumination strength:

Power measurements at the back focal plane revealed that the real power of the LED and Laser Combiner light sources (in mW) do not scale linearly over the complete range of set values and also varies with wavelength (Fig. 13). Mapping this relationship between set illumination power and the actual illumination power is useful for ensuring comparable illumination conditions across experiments during quantitative imaging.

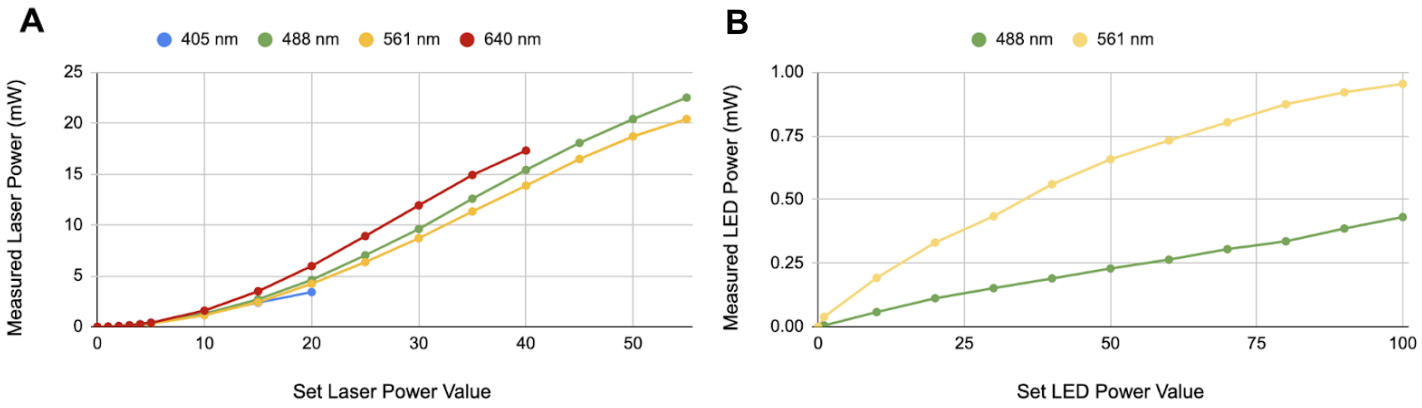

Fig. 13: Power measurements of the (A) laser combiner and (B) LED illumination sources at the back focal plane for different wavelengths

2. Camera gain:

The camera gain value is the factor used to convert the number of photoelectrons generated at each sensor pixel to the digital grey values in the captured image. Knowing the gain value allows one to compute the number of photoelectrons generated at the sensor on illumination by the sample. An sCMOS camera may also have pixel-to-pixel variation in the gain value. Thus, it is important to account for differences in the gain values across different parts of an image while performing quantitative microscopy. The gain value for each of the 1200x1200 pixels on the sCMOS camera sensor was computed to have a mean value of 1.704 ADU/electron, with a standard deviation of 0.062 (Fig. 14).

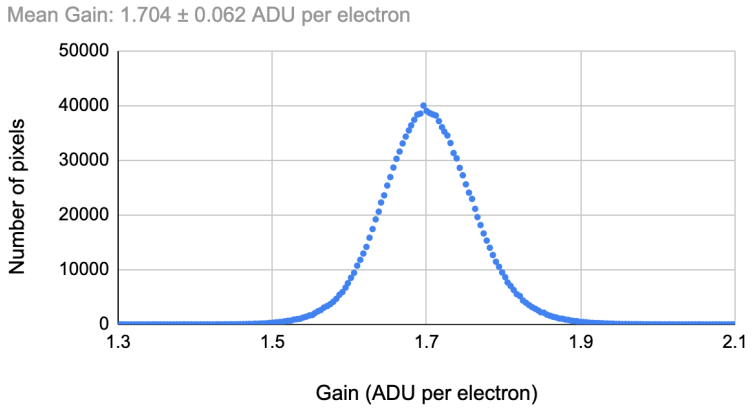

Fig. 14: Frequency distribution of gain values computed for the sCMOS camera sensor

3. Camera linearity and stability:

The performance of the sCMOS camera attached to the microscope was assessed by evaluating the stability and linearity of the signal it can capture from an autofluorescent plastic slide. The mean intensity of the signal captured by the camera was found to remain stable over a prolonged acquisition time of 2000 seconds (33 min), showing a fluctuation of 0.2% (Fig. 15A). The mean intensity of the signal also scaled linearly with exposure time (99.9% linearity, R^2=1) until the full well capacity of the sensor was reached (at over 500 ms exposure time) (Fig. 15B). Stability measurements were taken at a fixed illumination power and exposure time, while linearity measurements were taken at a fixed illumination power.

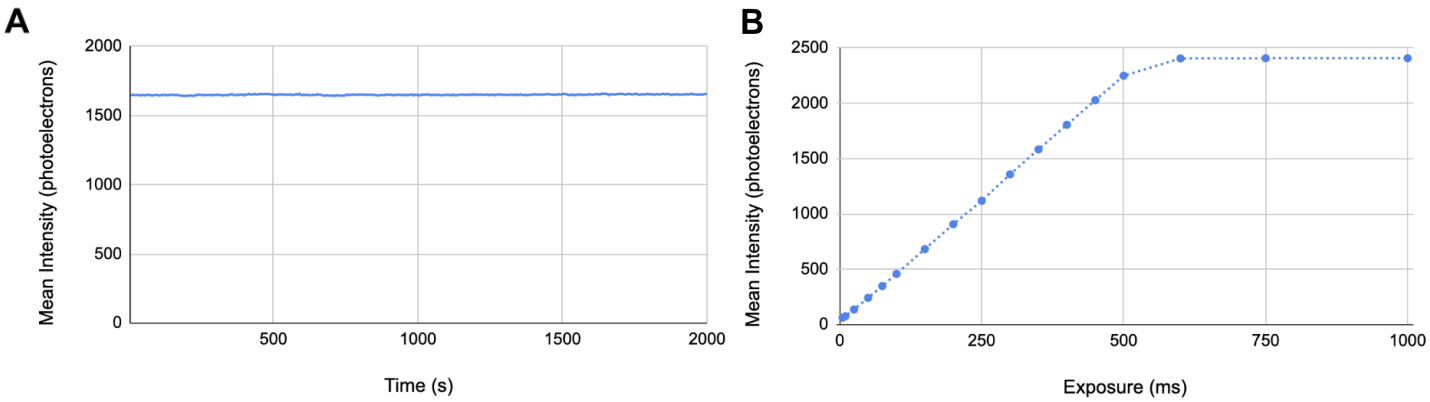

Fig. 15: The mean intensity of the signal captured by the camera remains stable over prolonged acquisition times (A) and scales linearly with exposure time (B)

4. Resolution:

The XY resolution of the 100x, 1.45 NA objective of the TIRF microscope was computed manually and with the PSFj software by imaging sub-resolution 100 nm TetraSpeck beads (Fig. 16) (Theer et al., 2014). The XY resolution calculated manually was 325 ± 26.5 nm (n=18 beads), which agrees with the value calculated by PSFj, 320 ± 2 nm (n=255 beads). These values are expected to differ from the theoretical XY resolution of 221 nm (resolution = 0.61λ/NA) due to imperfections in the lens and optical setup.

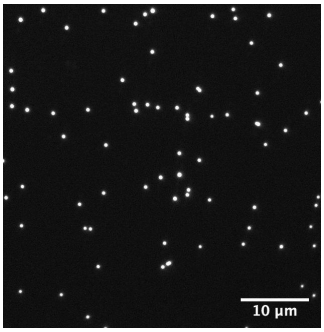

Fig. 16: 100 nM TetraSpeck beads imaged using a 100x, 1.45 NA objective and 1.5x tube lens

C. *In Vitro* Reconstitution of Membrane Tethered Minimal Actin Cortices

1. Creating freely diffusing supported lipid bilayers

Supported lipid bilayers composed of 98 mol % of DOPC with 2 mol % of DGS-NTA (Ni) were created on a glass coverslip and imaged using TIRF microscopy. This lipid composition was used for all subsequent experiments. The bilayers were visualised by labelled 10xHis-Snap-UtrophinABD linker proteins that tether to the Ni-chelated NTA lipids in the bilayer. The quality of the bilayer was evaluated by FRAP to determine the diffusion coefficient and mobile fraction of the UtrophinABD linker protein (Fig. 17A). The diffusion coefficient was computed using the effective bleach radius and half-life of recovery of the FRAP traces (see Materials and Methods) (Fig. 17B, 17D). The UtrophinABD linker proteins showed a mobile fraction of 0.96 ± 0.05 and a diffusion coefficient of 1.14 ± 0.13 um^2/s (n=5 FRAP traces across 3 bilayers), indicative of a freely diffusing bilayer (Fig. 17D). Proteins tethered to a freely diffusing supported lipid bilayer are expected to show a mobile fraction of at least 0.9 and a diffusion coefficient of 0.8-1.5 um^2/s (Koster et al., 2022).

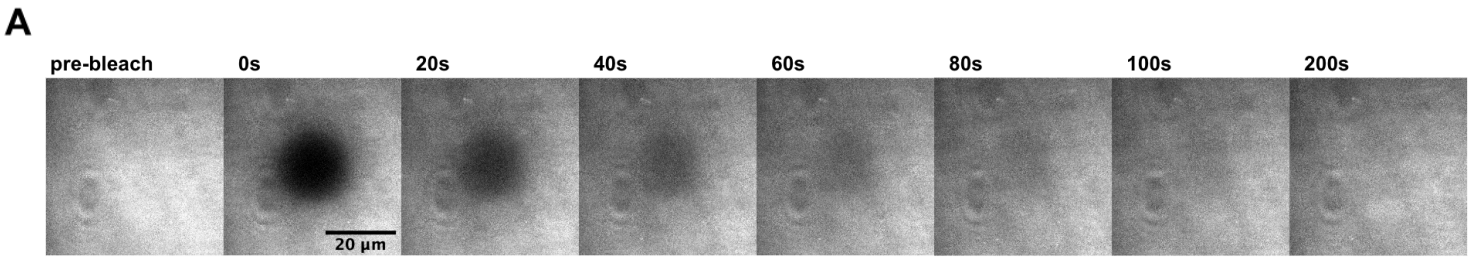

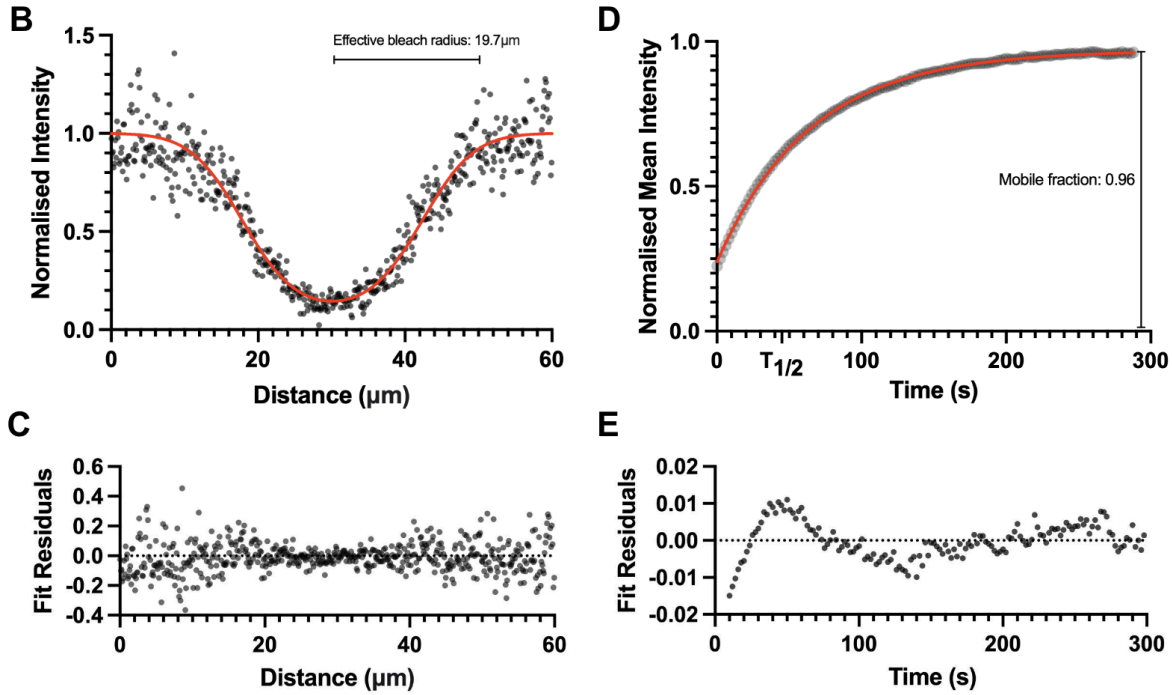

Fig. 17: (A) Representative snapshots of Fluorescence Recovery after Photobleaching of a 98:2 mol % DOPC:NTA-Ni supported lipid bilayer visualised by 10 nM of 10xHis-Snap-UtrophinABD linker protein. (B) Normalised line scan profile of the representative bleached spot fit to a Gaussian distribution to compute the effective bleach radius. (C) Residuals plot indicating goodness of the line scan profile fit. (D) Normalised recovery profile of the representative bleached spot fit to an exponential decay model to compute the half-life of recovery. (E) Residuals plot indicating goodness of recovery profile fit.

2. Reconstituting pre-polymerised actin filaments on a supported lipid bilayer

Pre-polymerised actin filaments of varying concentrations were then added to the supported lipid bilayer. These filaments were tethered to the bilayer by the UtrophinABD membrane-actin linker (Fig. 18A). As expected, the addition of actin filaments caused the distribution of the UtrophinABD linker protein to mirror the distribution of actin filaments across the bilayer (Fig. 18B). The effect of the addition of actin filaments on the diffusion of the UtrophinABD linker protein was evaluated by FRAP (Fig. 18C, 18D). The mobile fraction and the diffusion coefficient of the linker protein decreased with an increase in the concentration of actin filaments (Fig. 18E, 18F), following the same trend as reported by Koster et al., 2016. A concentration of 10 nM of actin filaments was found to be appropriate for observing single filaments (Fig. 18B) and was used for subsequent experiments to measure actin filament length (Fig. 19, 20).

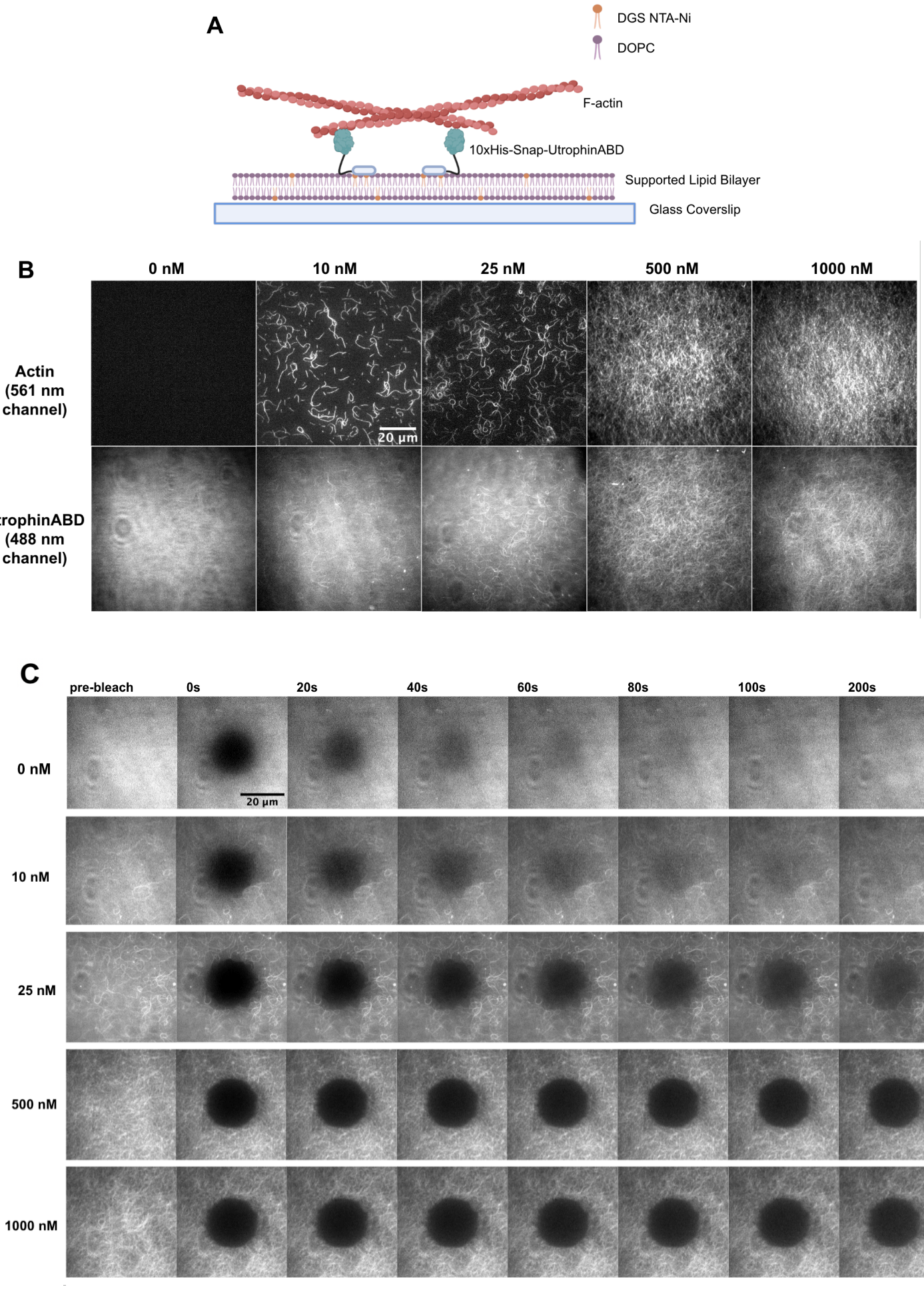
A
DGS NTA-Ni
DOPC
F-actin
10xHis-Snap-UtrophinABD
Supported Lipid Bilayer
Glass Coverslip
B
0 nM
10 nM
25 nM
500 nM
1000 nM
Actin (561 nm channel)
UtrophinABD (488 nm channel)
20 µm
C
pre-bleach
0s
20s
40s
60s
80s
100s
200s
0 nM
10 nM
25 nM
500 nM
1000 nM
20 µm

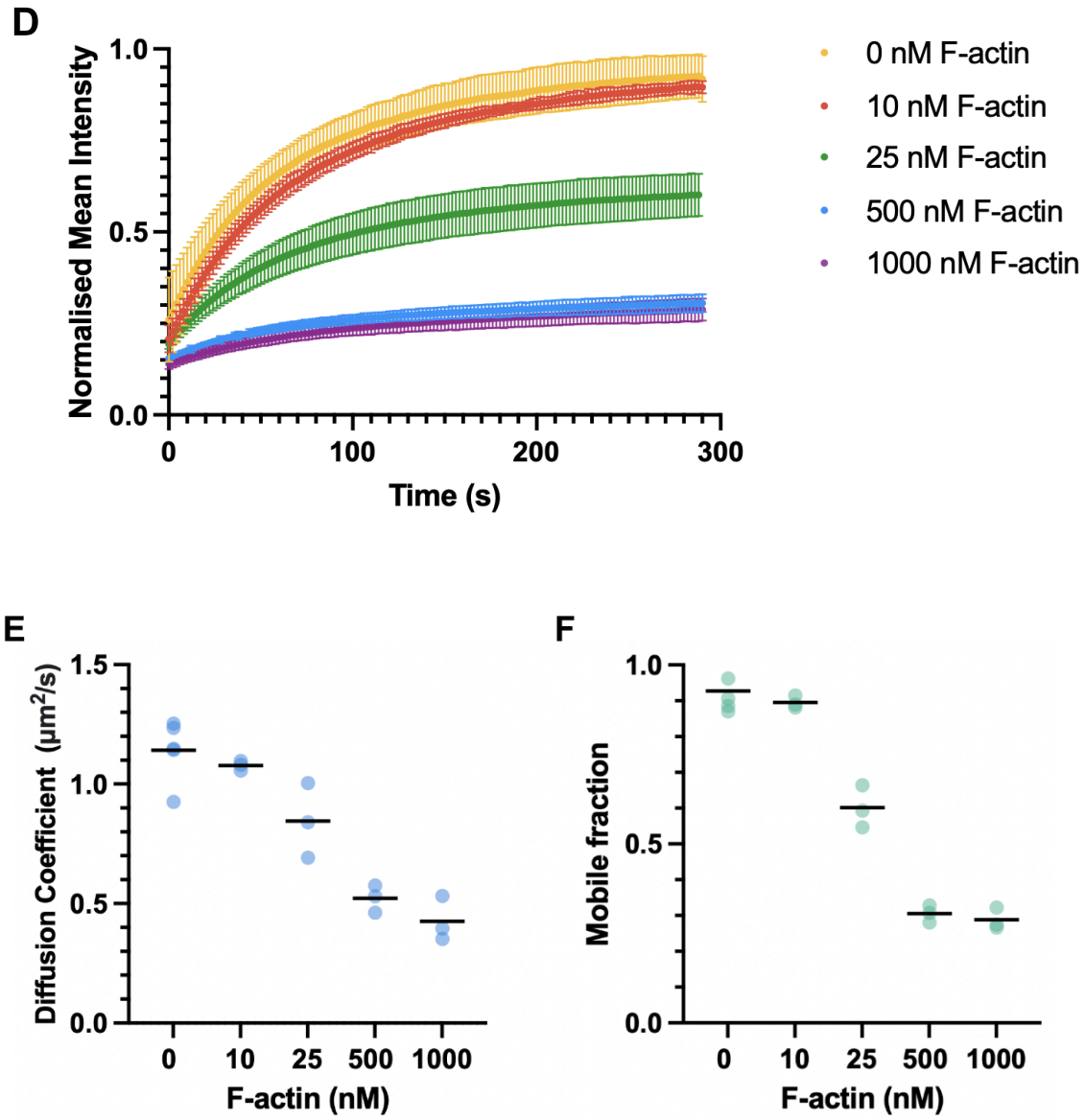

Fig. 18: (A) Schematic representation of pre-polymerised actin filaments tethered to a supported lipid bilayer via a UtrophinABD membrane-actin linker. (B) Images of varying concentrations of F-actin filaments tethered to a bilayer containing 10 nM UtrophinABD linker. (C) Representative snapshots of fluorescence recovery after photobleaching of the UtrophinABD linker protein on the bilayer with varying concentrations of bound F-actin. (D) Averaged normalised recovery profiles, (E) diffusion coefficients, and (F) mobile fractions of the UtrophinABD membrane-actin linker on the bilayer as a function of F-actin concentrations (n=5,3,3,3,3 FRAP traces for 0nM, 10 nM, 25 nM, 500 nM and 1000 nM F-actin concentrations respectively) (points: mean and error bars: SD in Fig. 18D; horizontal line: mean in Fig. 18E and 18F).

3. Characterising the length scale distribution of capped actin filaments

Next, varying concentrations of CapZ capping protein were used to generate pre-polymerised actin filaments of varying lengths. 10 nM of these filaments were added to a bilayer containing the UtrophinABD membrane-actin linker and imaged (Fig. 19A). The actin filament length was observed to decrease with an increase in capping protein concentration from 0 to 50 nM but didn't reduce beyond this on increasing capping protein concentration to 100 nM (Fig. 19B, 20). The filament length distribution observed at all CapZ concentrations follows the same trend previously reported by Koster et al., 2016.

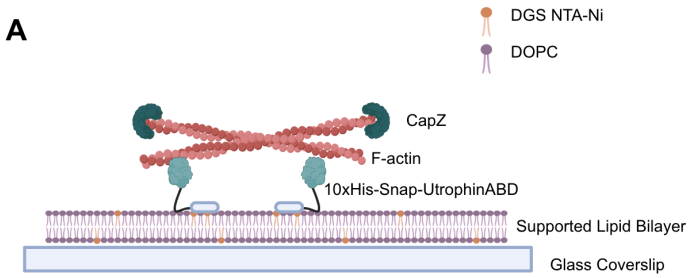

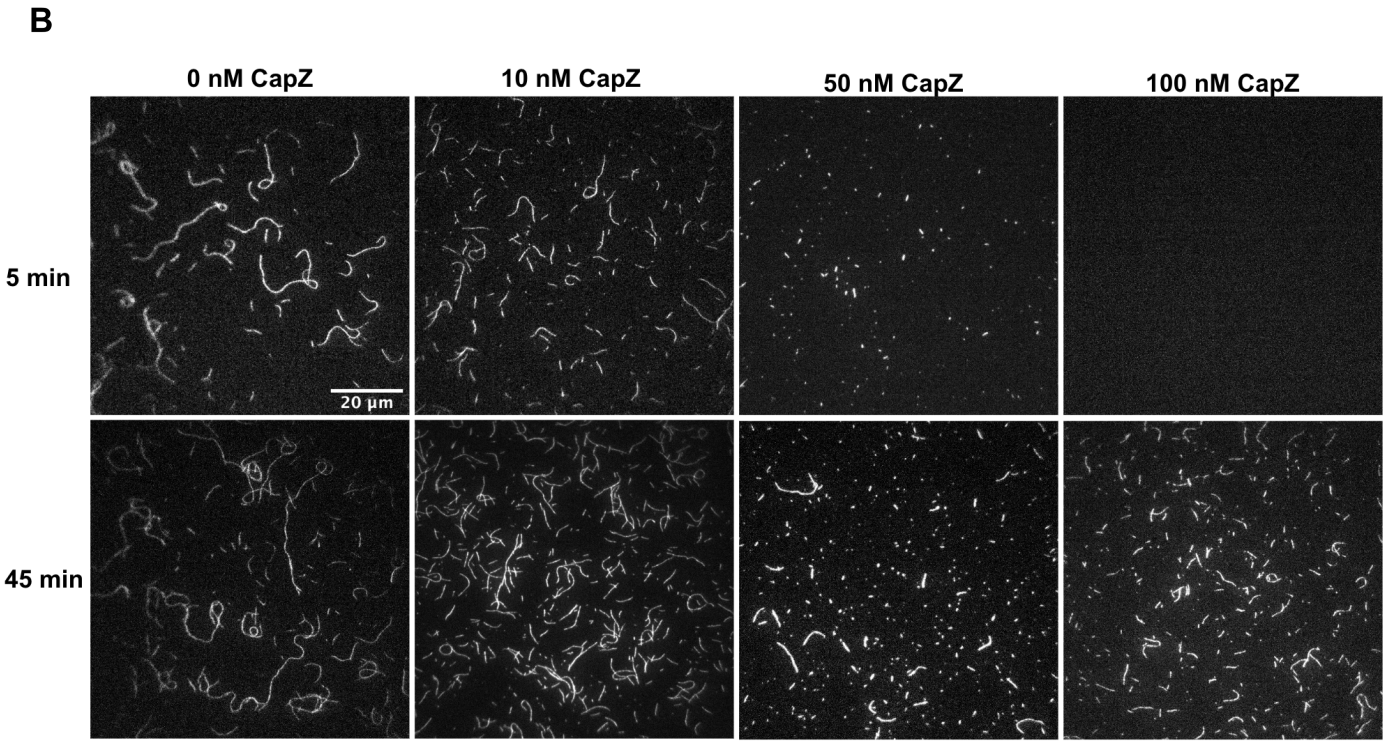

Fig. 19: (A) Schematic representation of pre-polymerised and capped actin filaments tethered to a supported lipid bilayer via a UtrophinABD membrane-actin linker. (B) Images of 10 nM of pre-polymerised actin filaments capped by varying amounts of CapZ capping protein taken 5 and 45 min after addition to a bilayer containing UtrophinABD linker proteins. Little to no actin filaments capped by 100 nM CapZ had tethered to the bilayer in the first 5 min

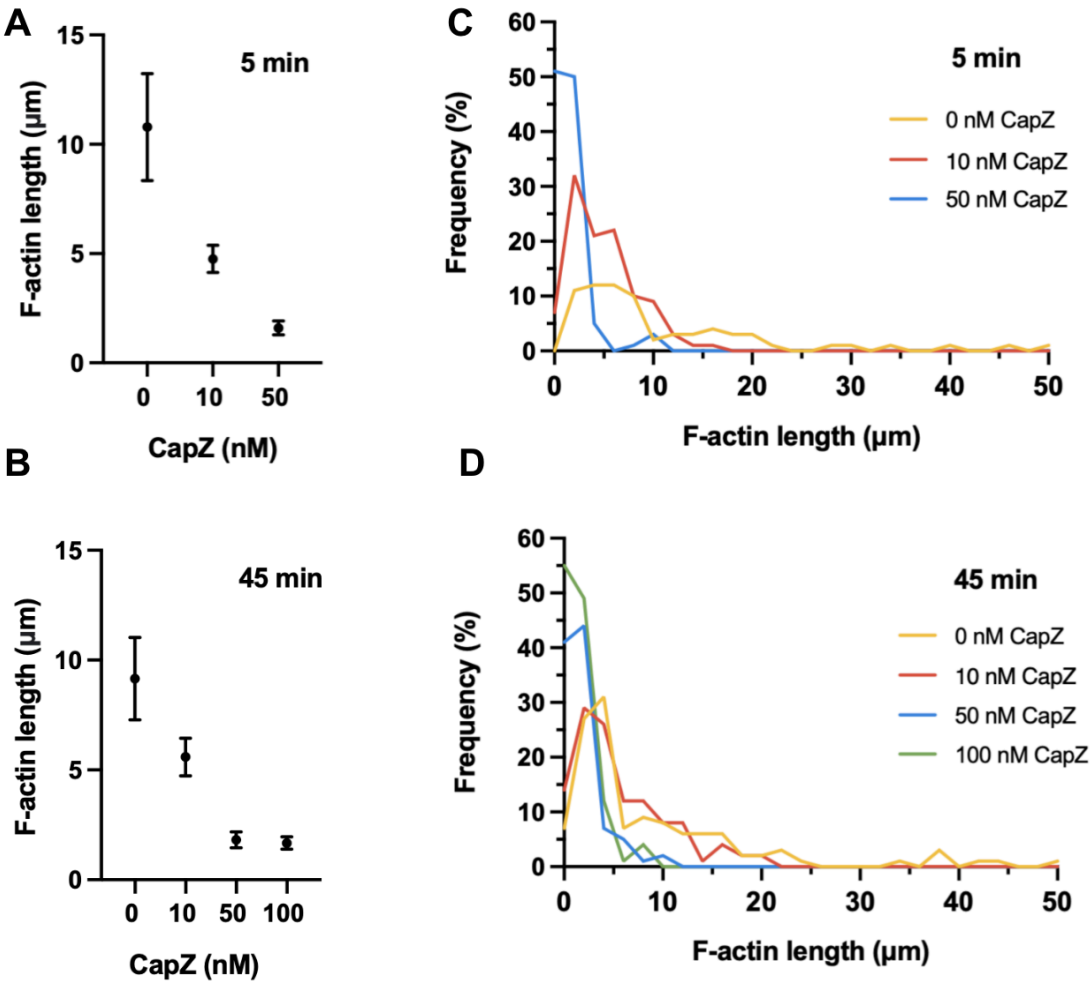

Fig. 20: Mean filament length of 10nM of pre-polymerised actin filaments capped by varying amounts of capping protein measured at (A) 5 min and (B) 45 min after addition to the supported lipid bilayer containing 10 nM 10xHis-Snap-UtrophinABD. Length scale distributions of the same filaments at (C) 5 min and (D) 45 min time points. Error bars: 95% CI. (n=70, 106, and 110 filaments for 0, 10 and 50 nM capZ concentrations at 5 min; n=123, 118, 100, and 118 filaments for 0, 10, 50 and 100 nM capZ concentrations at 45 min).

4. Evaluating elongation rates of actin filaments in the presence of formin and profilin

Finally, profilin and formin were used to spontaneously polymerise G-actin monomers into filaments on a supported lipid bilayer (Fig. 21). G-actin monomers were mixed with profilin in a 1:1.25 ratio and added to a supported lipid bilayer containing the UtrophinABD linker and formin. Many pre-nucleated filaments were observed to tether to the bilayer immediately after the mix was added, after which they appeared to spontaneously elongate in real-time. The elongation rate of these filaments increased with the concentration of G-actin-profilin added (Fig. 22, 23, 24) and was significantly lower in the absence of profilin (Fig. 22, 23, 24). However, no significant difference in the elongation rate was observed in the presence or absence of formin. Besides its role in nucleating filaments, formin is known to enhance filament elongation when present with profilin (Kovar et al., 2006; Funk et al., 2020; Pollard et al., 2020). This prompted the suspicion that the purified formin used may have been inactive.

In addition to pre-nucleated filaments, a small number of spontaneously nucleating filaments were observed on the bilayer (Fig. 25). These were distinguished by their spontaneous emergence, as well as their diminished brightness compared to pre-nucleated filaments of comparable size. The number of these spontaneously nucleating filaments was counted to determine if they were generated by formin activity. The number of these spontaneously nucleated filaments in a given area was similar in the presence and absence of formin, as was the total number of filaments (pre- and spontaneously nucleated) seen in either condition (Table 2). The elongation rate of spontaneously nucleated filaments was not significantly different in the presence or absence of formin (Fig. 26). Thus, the nucleation and elongation of filaments seem unaffected by the presence of formin, suggesting that the formin used may have been

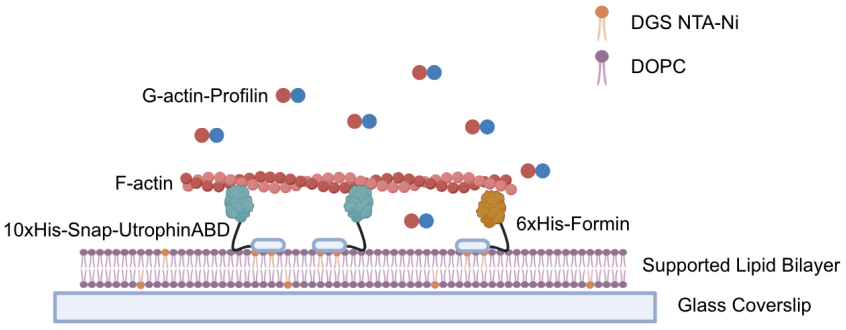

Fig. 21: Schematic representation of the reconstitution of spontaneously polymerising actin filaments using G-actin and profilin on a supported lipid bilayer containing UtrophinABD membrane-actin linkers and formin

inactive. However, more experiments need to be performed to validate the activity of formin.

.

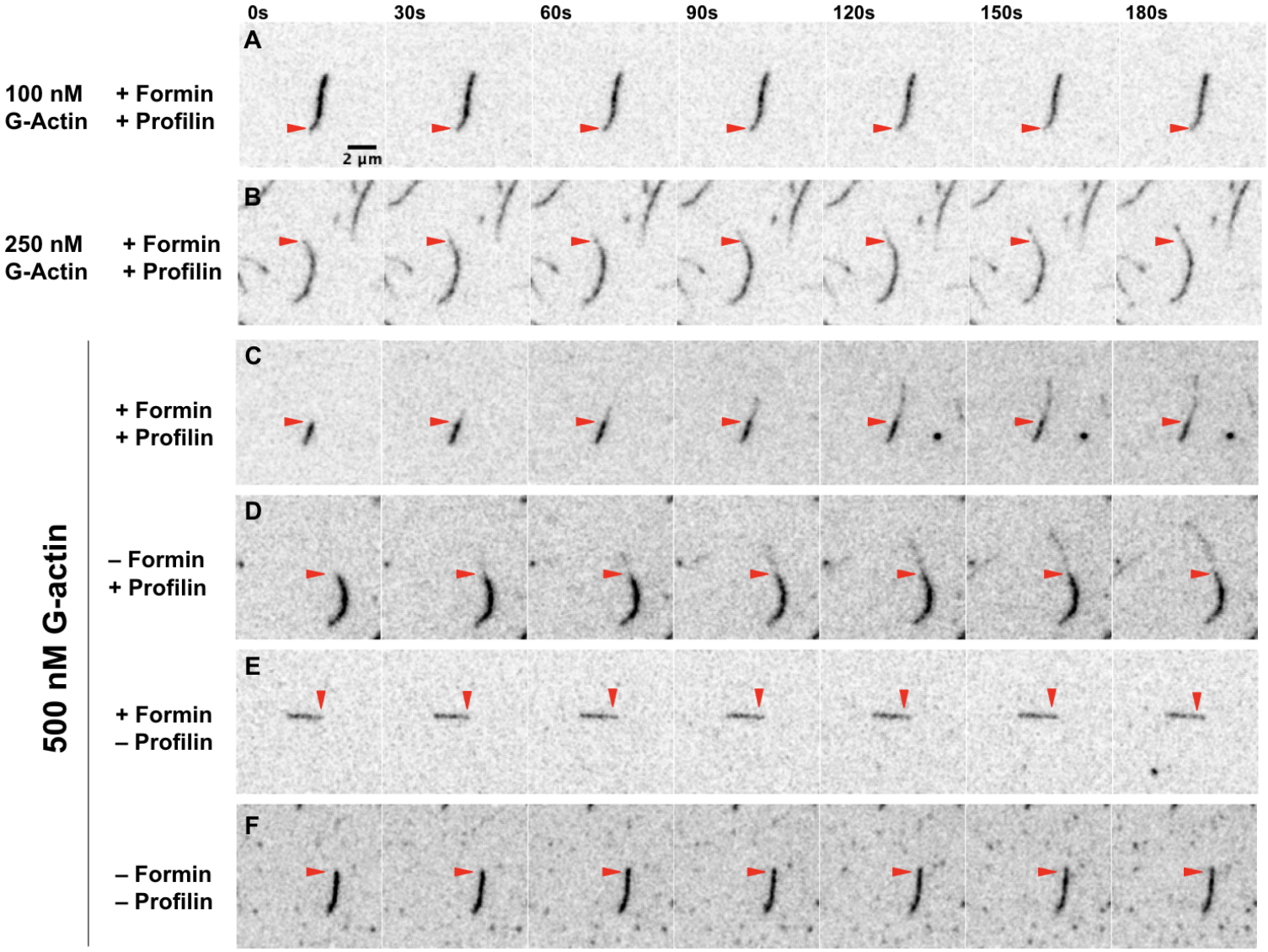

Fig. 22: Representative snapshots of pre-nucleated actin filament polymerisation on a supported lipid bilayer in the presence and absence of formin and profilin. (A) 100 nM, (B) 250 nM, and (C) 500 nM G-actin (20% labelled) were mixed with profilin in a 1:1.25 ratio and added to the bilayer containing 10 nM of the UtrophinABD membrane-actin liner and 10 nM formin. (D), (E) and (F) are negative controls for condition (C) having formin absent, profilin absent or both formin and profilin absent, respectively. Red arrows indicate the position of the growing end of actin filaments at t=0s.

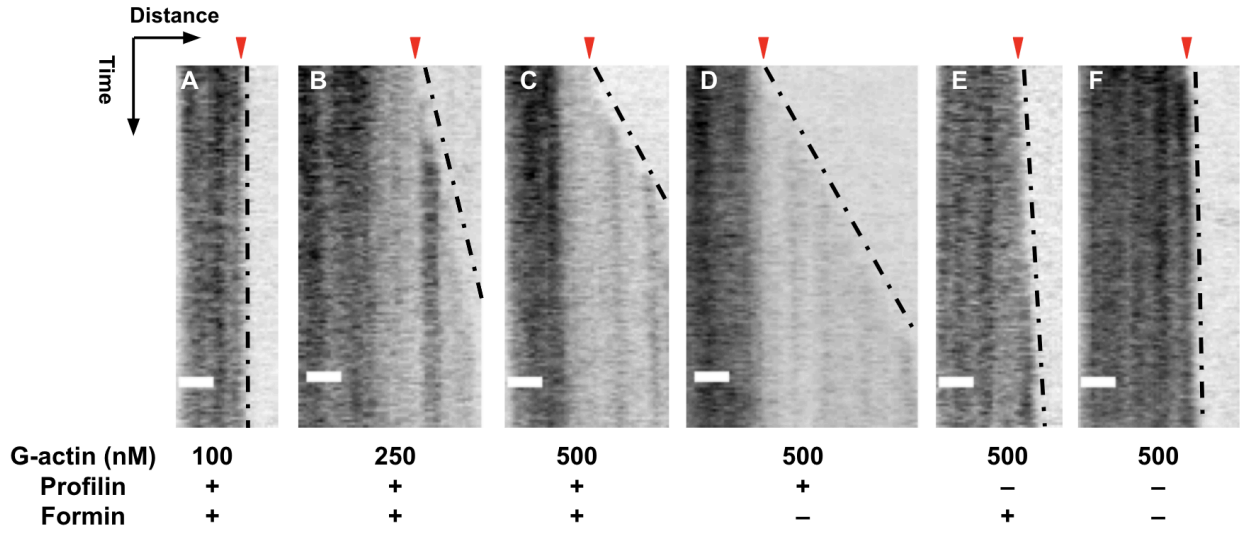

Fig. 23: Kymographs of actin filaments seen in Fig. 22. The x-axis represents distance, and the y-axis represents time. The red arrow indicates the edge of the filament at t=0s. The dotted line indicates the edge of the growing filament over time; its slope indicates the elongation speed. Scale bar: 1 µm. All kymographs represent a duration of 270s.

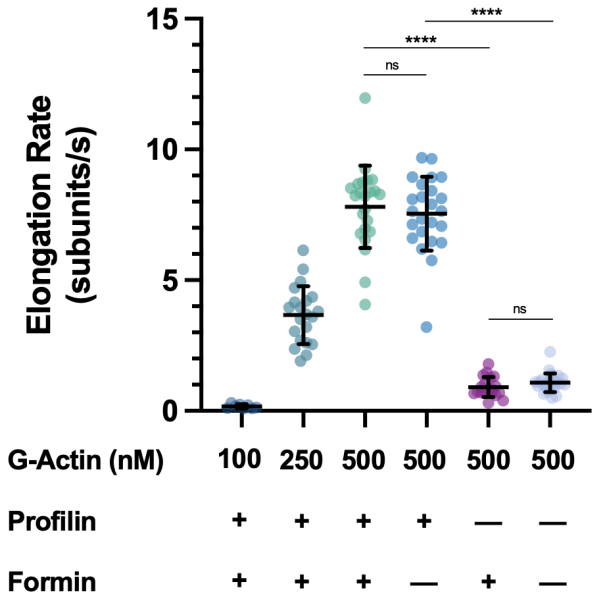

Fig. 24: Actin filament elongation rates measured in terms of actin subunits/s for the conditions represented by (A), (B), (C), (D), (E) and (F) in Fig. 22 and 23 (n= 8, 21, 23, 24, 18 and 25 filaments, respectively). Horizontal line: mean; whiskers: SD. Statistical significance was determined using the Mann-Whitney non-parametric t-test (ns: $p>0.05$; ****: $p<0.0001$)

	G-actin + Profilin	G-actin + Profilin + Formin	Fold Change
Total number of filaments	351	371	1.05
Number of spontaneously nucleated filaments	31	30	0.96

Table 3: Comparison of the number of actin filaments seen on the supported lipid bilayer over an area of 90 x 90 μm^2 in the presence and absence of formin.

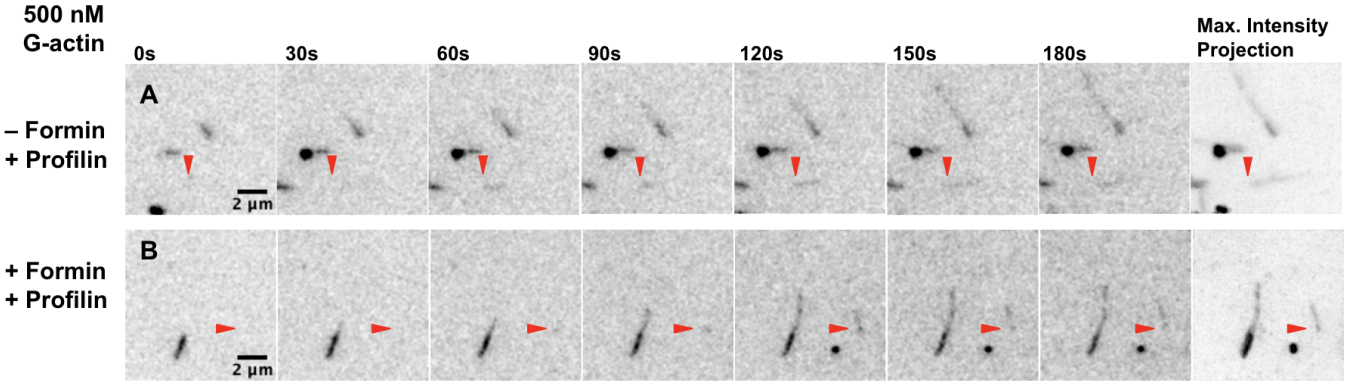

Fig. 25: Representative snapshots of the elongation of spontaneously nucleated filaments on a supported lipid bilayer in the (A) absence and (B) presence of formin. A maximum intensity projection across all frames of a 5 min long acquisition is included to depict the spontaneously nucleated filament clearly. The red arrow indicates the position of the filament on the bilayer.

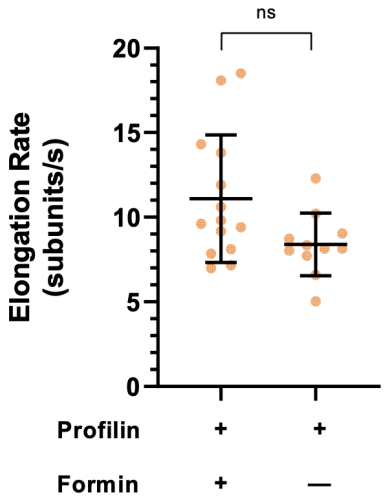

Fig. 26: Comparison of elongation rates of spontaneously nucleated filaments on the supported lipid bilayer in the presence and absence of formin (n=14 and 11 filaments, respectively). Horizontal line: mean; whiskers: SD. Statistical significance was determined using the Mann-Whitney non-parametric t-test (ns: $p>0.05$).

Previous studies have characterised actin filament polymerisation dynamics *in vitro* by using a variety of reconstitution set-ups and conditions. Funk et al., 2019 characterised actin filament elongation using bovine cytosolic β-γ actin in the presence and absence of human profilin 1 and mammalian formins (mDia1, mDia2 and DAAM1). They tethered elongating actin filaments to a flow chamber using phalloidin. Kovar et al., 2006, performed similar experiments using chicken muscle actin, fission yeast formin and profilin where growing filaments were tethered to a flow chamber using myosin II. Pollard et al., 2020, on the other hand, used budding yeast actin, profilin and formin in a set-up where filaments were nucleated by formin tethered to beads. The findings of these studies are summarised below (Table 3). The differences in the filament elongation rates measured in my experiments in comparison to these published values could be due to a number of reasons, including the activity of the purified proteins used, buffer conditions and the nature of the reconstitution setup. The most striking difference appears to be in the elongation rates of actin filaments in the absence of profilin and formin. More replicate experiments need to be performed to increase confidence in the elongation rates measured in this study.

	This study	Funk et al., 2020	Kovar et al., 2006	Pollard et al., 2020
G-Actin concentration	500 nM	500 nM, 1 µM	1 µM	1 µM
G-Actin: Profilin Ratio	1:1.25	1:1.5	1:5	1:1
Formin concentration	10 nM	15 nM	1 nM	-
Set-up	Filaments tethered to bilayer by UtrophinABD	Filaments tethered to flow chamber by phalloidin	Filaments tethered to flow chamber by myosin II	Filaments tethered to beads by formin
	Formin tethered to bilayer	Formin is not tethered	Formin is not tethered	Formin is tethered to beads
Actin kind	Chicken muscle	Bovine cytoplasmic (β-γ)	Chicken muscle	Budding yeast
Profilin kind	Fission yeast Cdc3	Human profilin1	Fission yeast profilin	Budding yeast Pfy1
Formin kind	Fission yeast Cdc12 (FH1-FH2)	Mouse mDia1 and 2; Human DAAM1	Fission yeast Cdc12 (FH1-FH2)	Budding yeast Bni1 (FH1-FH2)
Elongation Rates (subunits/s)				
G-Actin only	1.07 ± 0.36	4.1 ± 0.5 (500 nM actin); 11.1 ± 0.85 (1 µM actin)	10.9 ± 0.06	-
G-Actin + Profilin	7.54 ± 1.41	8.86 ± 0.18 (1 µM actin)	9.1 ± 0.1	-
G-Actin + Formin	0.9 ± 0.38	-	-	3.0 ± 1.6
G-Actin + Profilin + Formin	7.8 ± 1.58**	57.89 ± 5.64 (1 µM G-actin + mDia1) 31.96 ± 2.53 (1 µM G-actin + mDia2) 12.03 ± 1.23 (1 µM G-actin + DAAM1)	13.3 ± 0.6	17.5 ± 3.5

* Inferred value based on the linear relationship between G-actin-profilin concentration and elongation rates described in the study

** Formin is likely to have been inactive

Table 3: Comparison of actin filament elongation rates across studies

Chapter V: Discussion

In this thesis, I have attempted to set up an *in vitro* reconstitution system of a membrane-tethered minimal actomyosin cortex to study its role in driving local membrane organisation via active processes. With this system, the aim is to test whether non-muscle myosin II can generate contractile stresses on dynamic actin filaments, thereby clustering membrane components tethered to actin filaments, in line with previous evidence supporting the active-composite model of membrane organisation.

To build this system, I first required purified and activated non-muscle myosin II. Thus, I attempted to express the NMIIA and NMIIB isoforms of non-muscle myosin II as well as its activation partner, MLCK, in Sf9 cells by baculovirus infection. Thus, I generated recombinant bacmids encoding FLAG-tagged MLCK, NMIIA-HC and NMIIB-HC, along with untagged ELC and RLC, via site-specific transposition. These were validated by Sanger sequencing and PCR.

Subsequently, I generated P0 baculovirus stocks for all constructs by transfecting Sf9 cells with the recombinant bacmids. While the P0 stocks of MLCK, NMIIA-HC and RLC were virulent, P0 stocks of ELC and NMIIB-HC were not. P0 stocks of MLCK, NMIIA-HC and RLC were successfully amplified to generate P1 stocks of these constructs. However, when the P0 stocks of ELC and NMIIB-HC were added to Sf9 cultures, the cells showed no signs of infection. To troubleshoot this, I varied the P0 viral titre used for infection, prepared new P0 stocks by repeating transfection, and used P0 stocks generated from alternate copies of the recombinant bacmid. However, all attempts were unsuccessful. I suspect the ELC and NMIIB-HC bacmid DNA might be degraded or have deleterious mutations in essential viral genes. In which case, recombinant ELC and NMIIB-HC bacmids must be generated again.

I then tested FLAG-MLCK and FLAG-NMIIA-HC expression in baculovirus-infected Sf9 cells by western blot. Numerous degradation bands of FLAG-NMIIA-HC were detected,

which I anticipate will be minimised if NMIIA-HC is co-expressed with its stabilising light chains ELC and RLC. The expression of full-length FLAG-MLCK protein in Sf9 cells was also detected, and a majority of the protein was extracted into the soluble fraction of the lysate rather than the insoluble pellet.

Going forward, MLCK protein can now be purified from a larger culture volume of baculovirus-infected Sf9 cells by FLAG-tag-based affinity purification. Once viruses for RLC and NMIIB-HC are generated, Sf9 cells can be co-infected with ELC, RLC, and either NMIIA-HC or NMIIB-HC viruses to express the complete NMIIA or NMIIB protein. Once NMIIA, NMIIB and MLCK are purified by FLAG-based affinity chromatography, NMIIA and NMIIB may be activated *in vitro* by phosphorylation by MLCK. Functional NMIIA and NMIIB proteins can then be isolated by dead-head clearance, and their activity can be confirmed by *in vitro* motility assays (Tripathi et al., 2021). Finally, the contractility of the purified myosins can be tested with actin filaments and membrane-actin linkers on a supported lipid bilayer.

In my attempt to build a membrane-tethered minimal actomyosin cortex, I next reconstituted pre-polymerised actin filaments on a supported lipid bilayer. The actin filaments were tethered to the bilayer using actin-membrane linker proteins and imaged using TIRF microscopy as per protocols adapted from Koster *et al.,* 2022. Various properties of the TIRF microscopy set-up, including the power of the light sources, camera gain, camera linearity, camera stability and resolution of the objective, were characterised. Next, the effect of increasing the concentration of pre-polymerised actin filaments on the diffusion of the linker protein on the bilayer was characterised, reproducing the trend observed by Koster et al*.,* 2016. Additionally, the length scale distribution of single pre-polymerised actin filaments capped by varying concentrations of CapZ capping protein was characterised, again reproducing the trend observed by Koster et al*.,* 2016. Having reproducibly built this reconstitution system from individual components, I then attempted to adapt it to generate dynamic, actin filaments that spontaneously polymerise on the bilayer and image this process in real-time.

I reconstituted spontaneously polymerising actin filaments on a bilayer using G-actin and profilin. An increase in elongation rate was observed with an increase in G-actin-profilin concentration, as previously reported by others. However, the addition of formin to the bilayers did not result in increased nucleation or elongation of actin filaments. This is contrary to formin's known role in promoting filament nucleation and elongation (Breitsprecher et al., 2013). Thus, I suspect that the purified formin used may have been inactive. Spontaneously polymerising filaments that were pre-nucleated prior to addition to the bilayer or spontaneously nucleated on the bilayer are likely to have been generated due to actin's ability to spontaneously nucleate into filaments above its critical concentration of 100 nM. While profilin was always added in excess of G-actin, it may have been inadequate to completely prevent the nucleation of F-actin in the absence of formin.

More experiments need to be performed to validate the activity of the purified formin by titrating the concentration of formin added to the bilayer. Minimising spontaneous nucleation in the absence of formin would be necessary to better characterise the specific effects of formin in nucleating and elongating actin filaments. In future experiments, the amount of profilin used could be scaled up to minimise spontaneous nucleation of actin in the absence of formin. Thus, any filaments nucleated on the bilayer could be attributed to formin activity. Using fluorescently labelled formin would also allow one to look for the processive movement of formin along the growing actin filament.

Notably, in my experiments, elongating stretches of actin filaments appeared dimmer than the pre-nucleated seed filaments. It is possible that profilin may have a greater affinity for unlabelled G-actin monomers than labelled monomers, as previously reported (Kovar et al., 2006), resulting in dimmer elongating filaments in the presence of profilin. The diminished brightness of elongating filaments in the presence of formin was useful in distinguishing between spontaneously nucleating filaments and the tethering of pre-nucleated filaments of comparable size. However, the diminished brightness is an impediment to making accurate measurements of filament length. Using alternate

labelling methods (such as F-actin-binding LifeAct probes used by Funk et al., 2019) could improve the signal generated by polymerising actin filaments, allowing one to track changes in filament length more accurately and better account for random stage drift that occurs during image acquisition.

In the future, it would be necessary to explore alternative sample chamber designs in order to be able to scale up G-actin-profilin concentrations to match physiological values (which can be as high as 150 μM; Funk et al., 2019). It would also be more physiologically relevant to test cytoplasmic actin in future experiments rather than muscle actin. A key prediction of the active-composite model is the existence of shorter actin filaments (~250 nm) amongst the larger stable actin filaments of the cortex (Gowirshankar et al., 2012). To generate spontaneously polymerising filaments of such length *in vitro*, it would be necessary to add the F-actin severing protein, cofilin, or F-actin capping protein, CapZ, to the system along with G-actin, profilin, formin and UtrophinABD. Since the TIRF microscope is limited by an XY resolution of ~320 nM, it would be necessary to opt for alternative microscopy techniques like STED, which can achieve lower XY resolutions to visualise such short filaments.

In conclusion, I attempted to set up an *in vitro* reconstitution system to study the role of actomyosin in driving local membrane organisation. In this direction, I attempted to recombinantly express non-muscle myosin II and myosin light chain kinase in Sf9 insect cells. I also reconstituted pre-polymerised actin filaments of defined length (using capping proteins) as well as spontaneously polymerising actin filaments (using profilin) on a freely diffusing supported lipid bilayer. Future work would be directed towards optimising expression and purification of NMIIA, NMIIB and MLCK, as well as incorporating functional formin along with G-actin, profilin, cofilin and CapZ to generate a dynamically assembling and disassembling minimal actin cortex where the active clustering of membrane components can be tested.

References

Axelrod, D., Koppel, D. E., Schlessinger, J., Elson, E., & Webb, W. W. (1976). Mobility measurement by analysis of fluorescence photobleaching recovery kinetics. Biophysical journal, 16(9), 1055-1069 https://doi.org/10.1016/s0006-3495(76)85755-4

Bac-to-BacTM Baculovirus Expression System: An efficient site-specific transposition system to generate baculovirus for high-level expression of recombinant proteins USER GUIDE, Gibco, publication number: MAN0000414

Baumgart, T., Hammond, A. T., Sengupta, P., Hess, S. T., Holowka, D. A., Baird, B. A., & Webb, W. W. (2007). Large-scale fluid/fluid phase separation of proteins and lipids in giant plasma membrane vesicles. Proceedings of the National Academy of Sciences, 104(9), 3165-3170. https://doi.org/10.1073/pnas.0611357104

Bhat, A. (2023). Active actin flows drive the sorting of membrane proteins with differential actin-binding affinity. PhD Thesis submitted to NCBS, TIFR, Bangalore.

Breitsprecher, D., & Goode, B. L. (2013). Formins at a glance. Journal of cell science, 126(1), 1-7. https://doi.org/10.1242/jcs.107250

Bretscher, M. S. (1972). Asymmetrical lipid bilayer structure for biological membranes. Nature New Biology, 236(61), 11-12. https://doi.org/10.1038/newbio236011a0

Chugh, P., & Paluch, E. K. (2018). The actin cortex at a glance. Journal of cell science, 131(14), jcs186254. https://doi.org/10.1242/jcs.186254

Edidin, M. (2003a). Lipids on the frontier: a century of cell-membrane bilayers. Nature reviews Molecular cell biology, 4(5), 414-418. https://doi.org/10.1038/nrm1102

Edidin, M. (2003b). The state of lipid rafts: from model membranes to cells. Annual review of biophysics and biomolecular structure, 32(1), 257-283. https://doi.org/10.1146/annurev.biophys.32.110601.142439

Fujiwara, T., Ritchie, K., Murakoshi, H., Jacobson, K., & Kusumi, A. (2002). Phospholipids undergo hop diffusion in compartmentalized cell membrane. The Journal of cell biology, 157(6), 1071-1082. https://doi.org/10.1083/jcb.200202050

Funk, J., Merino, F., Schaks, M., Rottner, K., Raunser, S., & Bieling, P. (2021). A barbed end interference mechanism reveals how capping protein promotes nucleation in branched actin networks. Nature communications, 12(1), 5329. https://doi.org/10.1038/s41467-021-25682-5

Funk, J., Merino, F., Venkova, L., Heydenreich, L., Kierfeld, J., Vargas, P., ... & Bieling, P. (2019). Profilin and formin constitute a pacemaker system for robust actin filament growth. Elife, 8, e50963. https://doi.org/10.7554/elife.50963

Goswami, D., Gowrishankar, K., Bilgrami, S., Ghosh, S., Raghupathy, R., Chadda, R., ... & Mayor, S. (2008). Nanoclusters of GPI-anchored proteins are formed by cortical actin-driven activity. Cell, 135(6), 1085-1097. https://doi.org/10.1016/j.cell.2008.11.032

Gowrishankar, K., Ghosh, S., Saha, S., Rumamol, C., Mayor, S., & Rao, M. (2012). Active remodeling of cortical actin regulates spatiotemporal organization of cell surface molecules. Cell, 149(6), 1353-1367. https://doi.org/10.1016/j.cell.2012.05.008

Kaiser, H. J., Lingwood, D., Levental, I., Sampaio, J. L., Kalvodova, L., Rajendran, L., & Simons, K. (2009). Order of lipid phases in model and plasma membranes. Proceedings of the National Academy of Sciences, 106(39), 16645-16650. https://doi.org/10.1073%2Fpnas.0908987106

Kalappurakkal, J. M., Sil, P., & Mayor, S. (2020). Toward a new picture of the living plasma membrane. Protein Science, 29(6), 1355-1365. https://doi.org/10.1002/pro.3874

Kang, M., Day, C. A., Drake, K., Kenworthy, A. K., & DiBenedetto, E. (2009). A generalization of theory for two-dimensional fluorescence recovery after photobleaching applicable to confocal laser scanning microscopes. Biophysical journal, 97(5), 1501-1511. https://doi.org/10.1016/j.bpj.2009.06.017

Kang, M., Day, C. A., Kenworthy, A. K., & DiBenedetto, E. (2012). Simplified equation to extract diffusion coefficients from confocal FRAP data. Traffic, 13(12), 1589-1600. https://doi.org/10.1111/tra.12008

Kovács, M., Wang, F., Hu, A., Zhang, Y., & Sellers, J. R. (2003). Functional divergence of human cytoplasmic myosin II: kinetic characterization of the non-muscle IIA isoform. Journal of Biological Chemistry, 278(40), 38132-38140. https://doi.org/10.1074/jbc.m305453200

Kusumi, A., Fujiwara, T. K., Chadda, R., Xie, M., Tsunoyama, T. A., Kalay, Z., ... & Suzuki, K. G. (2012). Dynamic organizing principles of the plasma membrane that regulate signal transduction: commemorating the fortieth anniversary of Singer and Nicolson's fluid-mosaic model. Annual review of cell and developmental biology, 28, 215-250. https://doi.org/10.1146/annurev-cellbio-100809-151736

Kusumi, A., Sako, Y., & Yamamoto, M. (1993). Confined lateral diffusion of membrane receptors as studied by single particle tracking (nanovid microscopy). Effects of calcium-induced differentiation in cultured epithelial cells. Biophysical journal, 65(5), 2021-2040. https://doi.org/10.1016/s0006-3495(93)81253-0

Köster, D. V., Bhat, A., Talluri, S., & Mayor, S. (2022). Reconstitution of Membrane-tethered Minimal Actin Cortices on Supported Lipid Bilayers. JoVE (Journal of Visualized Experiments), (185), e63968. https://dx.doi.org/10.3791/63968

Köster, D. V., Husain, K., Iljazi, E., Bhat, A., Bieling, P., Mullins, R. D., ... & Mayor, S. (2016). Actomyosin dynamics drive local membrane component organization in an in vitro active composite layer. Proceedings of the National Academy of Sciences, 113(12), E1645-E1654. https://doi.org/10.1073/pnas.1514030113

Kovar, D. R., Harris, E. S., Mahaffy, R., Higgs, H. N., & Pollard, T. D. (2006). Control of the assembly of ATP-and ADP-actin by formins and profilin. *Cell*, *124*(2), 423-435. https://doi.org/10.1016/j.cell.2005.11.038

Lambert, T. J., & Waters, J. C. (2014). Assessing camera performance for quantitative microscopy. Methods in cell biology, 123, 35-53. https://doi.org/10.1016/B978-0-12-420138-5.00003-3

Lingwood, D., & Simons, K. (2010). Lipid rafts as a membrane-organizing principle. science, 327(5961), 46-50. https://doi.org/10.1126/science.1174621

Mayor, S., Bhat, A., & Kusumi, A. (2023). A survey of models of cell membranes: toward a new understanding of membrane organization. Cold Spring Harbor Perspectives in Biology, 15(10), a041394. https://doi.org/10.1101/cshperspect.a041394

Pardee, J. D., & Spudich, J. (1982). [18] Purification of muscle actin. In Methods in enzymology (Vol. 85, pp. 164-181). Academic Press. https://doi.org/10.1016/0076-6879(82)85020-9

Plowman, S. J., Muncke, C., Parton, R. G., & Hancock, J. F. (2005). H-ras, K-ras, and inner plasma membrane raft proteins operate in nanoclusters with differential dependence on the actin cytoskeleton. Proceedings of the National Academy of Sciences, 102(43), 15500-15505. https://doi.org/10.1073/pnas.0504114102

Pollard, T. D. (2016). Actin and actin-binding proteins. *Cold Spring Harbor perspectives in biology*, *8*(8), a018226. https://doi.org/10.1101/cshperspect.a018226

Pollard, T. D., Blanchoin, L., & Mullins, R. D. (2000). Molecular mechanisms controlling actin filament dynamics in nonmuscle cells. *Annual review of biophysics and biomolecular structure*, *29*(1), 545-576. https://doi.org/10.1146/annurev.biophys.29.1.545

Pollard, L. W., Garabedian, M. V., Alioto, S. L., Shekhar, S., & Goode, B. L. (2020). Genetically inspired in vitro reconstitution of Saccharomyces cerevisiae actin cables from seven purified proteins. *Molecular biology of the cell*, *31*(5), 335-347. https://doi.org/10.1091%2Fmbc.E19-10-0576

Pyrpassopoulos, S., Feeser, E. A., Mazerik, J. N., Tyska, M. J., & Ostap, E. M. (2012). Membrane-bound myo1c powers asymmetric motility of actin filaments. Current Biology, 22(18), 1688-1692. https://doi.org/10.1016/j.cub.2012.06.069

Quintanilla, M. A., Hammer, J. A., & Beach, J. R. (2023). Non-muscle myosin 2 at a glance. Journal of Cell Science, 136(5), jcs260890. https://doi.org/10.1242/jcs.260890

Raghupathy, R., Anilkumar, A. A., Polley, A., Singh, P. P., Yadav, M., Johnson, C., ... & Mayor, S. (2015). Transbilayer lipid interactions mediate nanoclustering of lipid-anchored proteins. Cell, 161(3), 581-594. https://doi.org/10.1016/j.cell.2015.03.048

Rao, M., & Mayor, S. (2014). Active organization of membrane constituents in living cells. Current opinion in cell biology, 29, 126-132. https://doi.org/10.1016/j.ceb.2014.05.007

Saha, S., Lee, I. H., Polley, A., Groves, J. T., Rao, M., & Mayor, S. (2015). Diffusion of GPI-anchored proteins is influenced by the activity of dynamic cortical actin. Molecular biology of the cell, 26(22), 4033-4045. https://doi.org/10.1091/mbc.E15-06-0397

Sellers, James R., and Sarah M. Heissler. "Nonmuscle myosin-2 isoforms." Current Biology 29, no. 8 (2019): R275-R278. https://doi.org/10.1016/j.cub.2019.03.022

Sengupta, P., Jovanovic-Talisman, T., Skoko, D., Renz, M., Veatch, S. L., & Lippincott-Schwartz, J. (2011). Probing protein heterogeneity in the plasma membrane using PALM and pair correlation analysis. Nature methods, 8(11), 969-975. https://doi.org/10.1038/nmeth.1704

Sezgin, E., Levental, I., Mayor, S., & Eggeling, C. (2017). The mystery of membrane organisation: composition, regulation and physiological relevance of lipid rafts. Nat. Rev. Mol. Cell Biol. https://doi.org/10.1038%2Fnrm.2017.16

Sharma, P., Varma, R., Sarasij, R. C., Gousset, K., Krishnamoorthy, G., Rao, M., & Mayor, S. (2004). Nanoscale organization of multiple GPI-anchored proteins in living cell membranes. Cell, 116(4), 577-589. https://doi.org/10.1016/s0092-8674(04)00167-9

Simons, K., & Ikonen, E. (1997). Functional rafts in cell membranes. nature, 387(6633), 569-572. https://doi.org/10.1038/42408

Singer, S. J., & Nicolson, G. L. (1972). The Fluid Mosaic Model of the Structure of Cell Membranes. Science, 175(4023), 720-731. https://doi.org/10.1126/science.175.4023.720

Spudich JA, Watt S (1971) The regulation of rabbit skeletal muscle contraction. I. Biochemical studies of the interaction of the tropomyosin-troponin complex with actin and the proteolytic fragments of myosin. J Biol Chem 246(15):4866–4871. https://doi.org/10.1016/S0021-9258(18)62016-2

Stam, S., Alberts, J., Gardel, M. L., & Munro, E. (2015). Isoforms confer characteristic force generation and mechanosensation by myosin II filaments. Biophysical journal, 108(8), 1997-2006. https://doi.org/10.1016/j.bpj.2015.03.030

Theer, P., Mongis, C. & Knop, M. PSFj: know your fluorescence microscope. Nat Methods 11, 981–982 (2014). https://doi.org/10.1038/nmeth.3102

Thoresen, T., Lenz, M., & Gardel, M. L. (2013). Thick filament length and isoform composition determine self-organized contractile units in actomyosin bundles. Biophysical journal, 104(3), 655-665. https://doi.org/10.1016/j.bpj.2012.12.042

Tripathi, A., Bond, C., Sellers, J. R., Billington, N., & Takagi, Y. (2021). Myosin-specific adaptations of in vitro fluorescence microscopy-based motility assays. *JoVE (Journal of Visualized Experiments)*, (168), e62180. https://doi.org/10.3791/62180

van Zanten, T. S., Cambi, A., Koopman, M., Joosten, B., Figdor, C. G., & Garcia-Parajo, M. F. (2009). Hotspots of GPI-anchored proteins and integrin nanoclusters function as nucleation sites for cell adhesion. Proceedings of the National Academy of Sciences, 106(44), 18557-18562. https://doi.org/10.1073/pnas.0905217106

Varma, R., & Mayor, S. (1998). GPI-anchored proteins are organized in submicron domains at the cell surface. Nature, 394(6695), 798-801. https://doi.org/10.1038/29563

Vicente-Manzanares, M., Ma, X., Adelstein, R. S., & Horwitz, A. R. (2009). Non-muscle myosin II takes centre stage in cell adhesion and migration. Nature reviews Molecular cell biology, 10(11), 778-790. https://doi.org/10.1038/nrm2786

Wang, F., Kovács, M., Hu, A., Limouze, J., Harvey, E. V., & Sellers, J. R. (2003). Kinetic mechanism of non-muscle myosin IIB: functional adaptations for tension generation and maintenance. Journal of Biological Chemistry, 278(30), 27439-27448. https://doi.org/10.1074/jbc.m302510200